Theses and Dissertations

2014

Nonlinear Magnetic Dynamics and The Switching Phase Diagrams in Spintronic Devices

Shu Anthoney Yan
University of South Carolina - Columbia

Nonlinear Magnetic Dynamics and The Switching Phase Diagrams in Spintronic Devices

by

Shu Yan

Bachelor of Science
Tongji University 2005

Master of Science
Tongji University 2008

_____

Submitted in Partial Fulfillment of the Requirements

for the Degree of Doctor of Philosphy in

Physics

College of Arts and Sciences

University of South Carolina

2014

Accepted by:

Yaroslaw Bazaliy, Major Professor

Richard Webb, Committee Member

Yuriy V. Pershin, Committee Member

Sophya V. Garashchuk, Committee Member

Lacy Ford, Vice Provost and Dean of Graduate Studies

www.manaraa.com

ACKNOWLEDGMENTS

I would like to give my sincere gratitude to my supervisor Professor Yaroslaw Bazaliy, for his valuable advice, patient guidance and support which made my study on the field of spintronics possible. His research intuition and experience inspired my great interest in spintronics and guided me through these years of Ph.D. studies. I am grateful to him for his creative thinking as well as insightful suggestions that is present at all times.

I would like to thank Professor Richard Webb, who is the head of the nano center. Your passion and enthusiasm for physics always inspire young generation in pursuing science as their careers. And we all sincerely wish you good health.

I would also like to thank Professor Yuriy Pershin and Professor Sophya Garashchuk for being my committee members and giving me many valuable comments and advices on my dissertation defence, and to thank all the members of the Condensed Matter Group, in particular Professor Thomas Crawford for many insightful suggestions you gave me in my research. I am also deeply grateful to Dr. Longfei Ye, one of my best friends in Physics Department, for your supports and many useful advices during my most miserable periods.

Finally, I would like to give my heartfelt thanks to my parents, who have raised me up and always care me the most. You are the person in the world who always support me and love me unconditionally. I'm so proud to have both of you as my parents and my best friends in life.

Abstract

Spin-transfer torque induced magnetic switching, by which the spin-polarized current transfers its magnetic moment to the ferromagnetic layer and changes its magnetization, holds great promise towards faster and smaller magnetic bits in data-storage applications due to the lower power consumption and better scalability.

We propose an analytic approach which can be used to calculate the switching phase diagram of a nanomagnetic system in the presence of both magnetic field and spin-transfer torque in an exact fashion. This method is applied to the study of switching conditions for the uniaxial, single domain magnetic layers in different spin-transfer devices. In a spin valve with spin polarization collinear with the easy axis, we get a modified Stoner-Wohlfarth astroid which represents many of the features that have been found in experiment. It also shows a self-crossing boundary and demonstrates a region with three stable equilibria. We demonstrate that the region of stable equilibria with energy near the maximum can be reached only through a narrow bottleneck in the field space, which sets a stringent requirement for magnetic field alignment in the experiments. Switching diagrams are then calculated for the setups with magnetic field not perfectly aligned with the easy axis.

In a ferromagnet-heavy-metal bilayer device with strong spin Hall effect, the in plane current becomes spin-polarized and transfers its magnetic moment to the ferromagnetic layer by diffusion. The three-dimensional asymmetric phase diagram is calculated. In the case that the external field is confined in the vertical plane defined by the direction of the current and the easy axis, the spin-transfer torque shifts the conventional in-plane (IP) equilibria within the same plane, and also creates two

out-of-plane (OOP) equilibria, one of which can be stable. The threshold switching currents for IP switching and OOP switching are discussed.

We also address the magnetic switching processes. Damping switching and precessional switching are two different switching types that are typically considered in recent studies. In the damping mode the switching is slow and heavily depends on the initial deviation, while in the precessional mode the accurate manipulation of the field or current pulse is required. We propose a switching scenario for a fast and reliable switching by taking advantage of the out-of-plane stable equilibrium in the SHE induced magnetic switching. The magnetization is first driven by a pulse of field and current towards the OOP equilibrium without precession. Since it is in the lower half of the unit sphere, no backwards pulse is required for a complete switching. This indicates a potentially feasible method of reliable ultra-fast magnetic control.

TABLE OF CONTENTS

List of Tables

List of Figures

CHAPTER 1

INTRODUCTION

Spintronics, a portmanteau meaning "spin transport electronics", is a term used to describe an emerging technology which merges magnetism and electronics by exploiting both the intrinsic spin of the electron and its associated magnetic moment, in addition to its fundamental electronic charge, in solid-state devices.

1.1 BACKGROUND

Spintronics emerged in the 1980s from discoveries concerning spin-dependent electron transport phenomena [32] and became a rapidly expanding area of research after the discovery of giant magnetoresistance (GMR), the significant change in resistance that occurs when the relative orientation of the magnetizations in two ferromagnetic layers changes, by Fert's group [4] and Grünberg's group [14] independently in 1988. The subsequent development of the device known as spin valve [18, 91] soon spurred interest at companies such as IBM to pursue research of ultra sensitive magnetic sensors for hard drive read heads. In 1997, IBM launched the first GMR based readout head, which soon became the standard technology for computer hard disks and prompted the hard disk data storage density to increase by roughly 100% per year. The practical significance of GMR effect was recognized by the Nobel Prize in Physics awarded to Fert and Grünberg in 2007.

After the discovery of GMR effect, several breakthroughs have further boosted this field, including the tunnel magnetoresistance (TMR) at room temperature in 1995 and the spin transfer effect in 1996. The TMR occurs in a magnetic tunnel junction

(MTJ) [57, 58], which consists of two ferromagnets separated by a thin insulator (typically a few nanometers). The dramatic improvement of magnetoresistance from the MTJ [64, 98, 97] further increases the storage capacity of modern hard disk drives and promotes realization of novel spintronics devices, such as the magnetoresistive random-access memory (MRAM) [2], a new type of non-volatile memory.

The phenomenon of spin-transfer is particularly attractive both from fundamental and applied points of view. In 1996 two independent theoretical studies by Slonczwski [73, 74] and Berger [11, 12] predicted a reciprocal reaction that accompanies the GMR effect in a metallic multilayer. The current flowing perpendicular to the plane in such multilayer structure can generate a torque strong enough to reorient the magnetization in one of the layers. Slonczwski proposed to characterize it as spin transfer, and predicted that such torque could generate two different types of magnetic behaviors depending on the device design and the magnitude of the current as well as an applied field: a steady precession driven by a constant current, and magnetization reversal driven by a pulsed current. Following this prediction, measurements of current-induced resistance changes in magnetic multilayer devices were identified with spin-torque-driven excitations by Tsoi et al., in point contact devices [84], and by Sun in manganite trilayer junctions [80]. Shortly afterwards, the spin torque induced magnetization reversal was observed in lithographically defined nanopillars [61, 35, 39] and in tunnel junctions [29, 22], which have spurred extensive study in metallic spin valve and MTJ nanopillar structures. Meanwhile, this subject has also attracted considerable theoretical studies and numerical simulations [78, 82, 93, 94, 34, 81].

In addition to the intrinsic scientific interest, the promising applications of spin-transfer torques also provide the impetus for many emerging spintronic technologies, including spin-transfer torque magnetic random access memories (STT-MRAMs). In conventional implementations of MRAM, in which the magnetic bits are switched

2

by Oersted fields, the long range of the magnetic fields limits the size of a single bit and places strict manufacturing constraints on the devices for reliable switchings. Since the spin-transfer effect can induce more reliable magnetization reversal in even smaller magnetic memory cells, the possibility that it could replace the Oersted fields due to this technology advantage has inspired a significant amount of research on this effect. Besides enhancing the switching efficiency for in-plane magnetized elements [8, 87, 7, 31, 41, 86, 15], several approaches have been put forward to design elements with perpendicularly magnetized magnetic layers for its lower switching current and better stability against thermal activation down to nanomagnet sizes [50, 71, 101, 51, 10, 43, 69, 30].

The phase diagrams observed in those studies contain several distinct types of precessional modes and static magnetic states [50, 51, 85, 42]. The magnetic dynamics in the present of spin-transfer torque is often understood in terms of the picture of power received or dissipated in a macrospin system [68, 17]. This approach provides intuitive understanding on magnetization reversals induced by spin-transfer torque. However, in the viewpoint of energy dissipation, the valid solution can only be obtained in the case that both the external field and the spin polarization are collinear with the magnetic easy axis. The complete phase diagram of a nanomagnet with uni-axial magnetic anisotropy, which exhibits strong distortion near the directions of easy axis, was first time measured experimentally by Y. Henry et al. in 2009 [26]. In the study of the distorted phase diagram, Y. Henry et al. modeled the effect by confining the equilibria in a plane under small current approximation. Although the extension of the Stoner-Wohlfarth model reflects some of the features of the current-distorted astroid, it fails to distinguish the different switching mechanisms [77] and therefore is not able to capture many of the features, especially near the easy axis where the out-of-plane shifts of equilibria become significant. One of the consequences is that the spin-transfer assisted metastable state, which has been observed experimentally,

3

www.manaraa.com

is actually prohibited in this model [42].

Because of the deficiency in the approximated models, we proposed an exact approach which is directly derived from the dynamic equation by disregarding the picture of energy landscape. Therefore it is suitable to calculate the phase diagrams in any magnetic systems in the presence of nonconservative forces. By applying it to a nanomagnet with uniaxial magnetic anisotropy subject to a current polarized along the easy axis, we show that the resulting phase diagrams capture the different switching scenarios induced by spin-transfer torque and also the feature that the equilibria are out of plane [96]. The switching phase diagram in the case with the external field applied slightly misaligned with the free layer easy axis successfully explains the experimental observations [50, 51, 85, 42].

Besides spin filter effects in devices such as spin valves or MTJs, spin Hall effect (SHE) is also a candidate that can be used in the field of spin injection, manipulation and detection [33]. Recent studies in bilayer nanowires consisting of a ferromagnetic layer and a heavy-metal layer with strong spin-orbit coupling have demonstrated efficient switching of magnetic layers [54, 45, 47], like those used in STT-MRAM, and efficient current-driven domain wall motion [56]. Two pictures have been taken into account to describe the magnetic dynamics, which separates the SHE induced torques into two terms, damping-like and field-like. However, the magnetic switching is believed to be induced by the damping-like torque only due to the geometry. The phase diagram in such systems is of importance in examining the theoretical prediction with the experiment measurement. Using the same approach, we calculate the complete phase diagram in three-dimension [95]. Different from the spin valve with the polarizer pointing in the same direction with the free layer easy axis, the geometry of SHE induced spin polarized current generates two additional OOP equilibria, one of which could be a stable sink. The property of this OOP equilibrium provides a possible solution for fast and reliable magnetization switching.

This dissertation focuses on the construction of the phase diagrams of nanomagnetic systems in the presence of spin-tranfer torques with different geometry. It also covers the dynamics of magnetic switching.

Chapter 2 gives an introduction of micromagnetism and a brief review of the spin transfer torques in GMR devices. The Landau-Lifshitz-Gilbert (LLG) equation, which describes the dynamics of magnetic systems, is covered in section 2.4. The spin transfer toque in a GMR device and the Landau-Lifshitz-Gilbert-Slonczewski (LLGS) equation is discussed in section 2.5.

Chapter 3 focuses on the general description of the switching phase diagrams for a single domain nanomagnet. In section 3.1 we briefly review the Stoner-Wohlfarth model and point out the limitation of the existing approach from the viewpoint of energy dissipation for calculating the critical surfaces. In section 3.2 we briefly review the classification of asymptotic behaviors for a linear planar system in general. Based on it, in section 3.3 we give a general description of the problem and the procedures to construct the critical surfaces for an arbitrary magnetic system in the presence of a spin transfer torque.

As our first application, the construction and analysis of the switching phase diagram for a spin valve nanopillar is described in Chapter 4. The different switching modes are analyzed in section 3.4. A novel region in the phase diagram is found in our result which has not yet been observed in experiment. In section 3.5 we construct the phase diagram in the case of a slightly misaligned axial field to account for the rotational symmetry breaking and compare with the phase diagrams calculated using the approximated method and those measured in experiments.

In Chapter 5, we study the switching phase diagram for a SHE bilayer nanowire. In addition to the shifts of the existing equilibria, the spin-transfer torque in this geometry also creates two out-of-plane (OOP) equilibria. The complete switching

phase diagram and the stability of the two OOP equilibria are discussed in section 5.3. In section 5.4 we derive the critical switching current for both in-plane switching and out-of-plane switching.

In Chapter 6 we focus on the magnetization dynamics. The two common magnetization switching strategies are described in section 6.1 and 6.2, respectively. In section 6.3 we propose a new switching scenario that takes advantage of the OOP equilibrium, indicating a potentially feasible method for reliable ultra-fast magnetic reversal.

The conclusions of the dissertation are summarized in Chapter 7.

Chapter 2

Nanoscale Magnetism and Spintronics

2.1 The origin of ferromagnetism

Ferromagnetism is the ability of some materials to display a macroscopic magnetization in the absence of external magnetic fields. The spin of the electrons in atoms is the main source of ferromagnetism, although the orbital angular momentum of the electrons may contribute as well. In atoms with a partially filled electron shell, the first few electrons in a shell tend to maximize the spin to minimize the energy in accordance with Hund's first rule, thereby increasing the total dipole moment. When these atoms form solids, however, electron states on neighboring atoms hybridize and form bands which suppress the formation of magnetic moments by inhibiting spin polarization. Therefore most solids are not ferromagnetic. Nevertheless, in a few transition metals with tightly bound 4f-orbitals, such as iron, cobalt, nickel, and their alloys, the exchange interaction is so strong that those levels tend to align spontaneously as they do in the atomic state, even when there is no applied field. This spontaneous magnetization effect is called ferromagnetism.

Although the exchange interaction keeps spins aligned, it does not align them in a particular direction. There are several kinds of magnetic anisotropy, the most common of which is magnetocrystalline anisotropy. This is a dependence of the energy on the direction of magnetization relative to the crystallographic lattice. Another common source of anisotropy, inverse magnetostriction, is induced by internal strains. Single-domain magnets also can have a shape anisotropy due to the magne-

tostatic effects of the particle shape. As the temperature of a magnet increases, the anisotropy tends to decrease, and there is often a blocking temperature, called the Curie temperature, at which a transition to superparamagnetism occurs [1].

2.2 MICROMAGNETICS

The length scales of interest in magnetic studies are usually much longer than atomic lengths, yet small enough to take into account the spatially non-uniform magnetization distribution. In this case atomic scale calculations become impractical and micromagnetics, a continuum description much like elasticity theory, models such non-uniformities in an efficient way. Micromagnetics can deal with static equilibria, by minimizing the magnetic energy, and with dynamic behavior, by solving the time-dependent dynamical equation.

In equilibrium, the magnetization direction aligns itself with an effective field. Generally, there are four main contributions to this effective field, which vary as a function of position: the externally applied magnetic field, the magnetocrystalline anisotropy, the micromagnetic exchange, and the magnetostatic field. Each of the fields can be described in terms of an associated contribution to the free energy. The magnetocrystalline anisotropy arises from the spin-orbit interactions and tends to align the magnetization with particular lattice directions. It is often written as a local function of the magnetization direction and has a different functional form for different lattices and materials. The micromagnetic exchange is the interaction that tends to keep the magnetization aligned in a common direction, adding an energy cost when the magnetization rotates as a function of position. The magnetostatic interaction is a highly non-local interaction between the magnetization at different points mediated by the magnetic field produced by the magnetization. Together, the

8

four free energies can be written as [1, 68]

$$E = -\mu_0 \int \mathrm{d}^3 r \mathbf{H}_{\text{ext}} \cdot \mathbf{M}(\mathbf{r}) - \frac{K_u}{M_s^2} \int \mathrm{d}^3 r (\mathbf{M}(\mathbf{r}) \cdot \mathbf{n})^2 + \frac{A_{\text{ex}}}{M_s^2} \int \mathrm{d}^3 r \sum_i \left(\frac{\partial}{\partial r_i} \mathbf{M} \right)^2$$
$$- \frac{\mu_0}{8\pi} \int \mathrm{d}^3 r \int \mathrm{d}^3 r' \mathbf{M}(\mathbf{r}) \cdot \frac{3(\mathbf{M}(\mathbf{r}') \cdot \mathbf{x})\mathbf{x} - \mathbf{M}(\mathbf{r}')|\mathbf{x}|^2}{|\mathbf{x}|^5}, \quad (2.1)$$

where K_u is the anisotropy constant, A_{ex} is the exchange constant, $\mathbf{n}$ is the direction of the uniaxial anisotropy easy axis, and $\mathbf{x} = \mathbf{r} - \mathbf{r}'$ is the vector between two sites. The magnetization $\mathbf{M}$ can vary internally but at each point its magnitude is equal to the saturation magnetization M_s.

The total effective field is then the functional derivative of the free energy with respect to the magnetization

$$\mu_0 \mathbf{H}_{\text{eff}}(\mathbf{r}) = -\frac{\delta E}{\delta \mathbf{M}(\mathbf{r})}. \quad (2.2)$$

The explicitly expression of the effective field derived from Eq. 2.1 is

$$\mathbf{H}_{\text{eff}}(\mathbf{r}) = \mathbf{H}_{\text{ext}} + \frac{2K_u}{\mu_0 M_s^2}(\mathbf{M}(\mathbf{r}) \cdot \mathbf{n})\mathbf{n} + \frac{2A_{\text{ex}}}{\mu_0 M_s^2}\nabla^2 \mathbf{M}$$
$$- \frac{1}{4\pi} \int \mathrm{d}^3 r' \frac{3(\mathbf{M}(\mathbf{r}') \cdot \mathbf{x})\mathbf{x} + \mathbf{M}(\mathbf{r}')|\mathbf{x}|^2}{|\mathbf{x}|^5}, \quad (2.3)$$

The atomic-like exchange, which drives the formation of the magnetization and which is not explicit in these expressions, places a strong energetic penalty on deviations of the magnitude of $\mathbf{M}(\mathbf{r})$ away from M_s. This interaction is generally taken into account by treating $\mathbf{M}(\mathbf{r})$ as having the fixed length M_s.

2.3 MACROSPIN APPROXIMATION

The macrospin approximation is applied to nanomagnet which are single-domain. In the framework of macrospin, the magnetization is treated as a single spin and we assume that the modulus of the magnetization is a constant. Since the free layer only evolves on the unit sphere surface, it removes one degree of freedom and the three components Cartesian coordinates can be replaced by spherical coordinates.

9

The energy anisotropy of a nanomagnet in the macrospin approximation is usually composed of two terms: magnetocrystalline anisotropy energy and magneostatic energy

$$E_{\text{an}} = -\frac{K_u V}{M_s{}^2} (\mathbf{M} \cdot \mathbf{n})^2 - \mu_0 V \mathbf{H}_d \cdot \mathbf{M}, \tag{2.4}$$

where V is the volume of the nanomagnet, and the demagnetizing field $\mathbf{H}_d = -\mathcal{N}_d \cdot \mathbf{M}$. The demagnetization tensor $\mathcal{N}_d$ depends on the shape of the nanomagnet and in a symmetric shape it is a diagonal matrix.

For a thin planar elliptical nanopillar with the plane normal chosen to coincide with the crystalline axis of the ferromagnet, these two terms can be combined together as an effective anisotropy. The simplest case is called uniaxial anisotropy, which can be written as:

$$E_{\text{an}} = -\frac{KV}{M_s{}^2} (\mathbf{M} \cdot \mathbf{n})^2 = -KV \cos^2 \theta, \tag{2.5}$$

where K is the effective anisotropy constant, and θ the angle between the easy axis and the particle's magnetization. The model that describes a single domain magnetic particle with uniaxial anisotropy is called Stoner-Wohlfarth model [79].

The energy landscape of a Stoner-Wohlfarth particle can be written in the format as follows

$$E = -\frac{KV}{M_s{}^2} (\mathbf{M} \cdot \mathbf{n})^2 - \mu_0 V \mathbf{H}_{\text{ext}} \cdot \mathbf{M}. \tag{2.6}$$

Any magnetocrystalline anisotropy and shape anisotropy can be included in the energy landscape by modifing the effective anisotropy in Eq. (2.5). For simplicity, however, we only consider the uniaxial anisotropy in this dissertation.

2.4   Landau-Lifshitz-Gilbert equation

The Landau-Lifshitz-Gilbert (LLG) equation describes the rotation of the magnetization in response to torques. Landau and Lifshitz first introduced the equation of
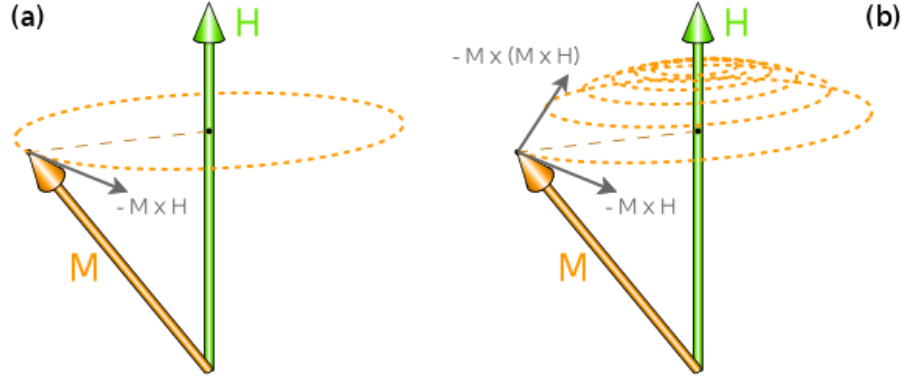
Figure 2.1: Illustration of the Landau-Lifschitz equation. (a) The magnetization precesses around the effective field without damping. (b) The magnetization precesses with Gilbert damping term towards the energy minimum state of the system.

motion for the magnetic moment in 1935

$$\frac{1}{\mu_0}\frac{\mathrm{d}\mathbf{M}}{\mathrm{d}t} = -\gamma\mathbf{M}\times\mathbf{H}_{\text{eff}} + \lambda\mathbf{M}\times(\mathbf{M}\times\mathbf{H}_{\text{eff}}), \tag{2.7}$$

where $\mathbf{H}_{\text{eff}}$ is the total effective field, γ is the electron gyromagnetic ratio. and λ is a phenomenological damping parameter, often replaced by $\lambda = -\alpha\gamma/M_s$. The visualisation of damped and undamped LL dynamics are shown in figure 2.1.

Since the damping of the magnetization motion in Landau-Lifshitz (LL) equation could not account for the large noneddy-current damping in the Permalloy sheets, in 1955, Gilbert replaced the damping term in the LL equation by one that depends on the time derivative of the magnetic field to take large damping into account [24]:

$$\frac{\mathrm{d}\mathbf{M}}{\mathrm{d}t} = -\gamma\mu_0(\mathbf{M}\times\mathbf{H}_{\text{eff}}) + \frac{\alpha}{M_s}\left(\mathbf{M}\times\frac{\mathrm{d}\mathbf{M}}{\mathrm{d}t}\right), \tag{2.8}$$

However, when the damping is not very high, the two forms are essentially equivalent. In the following chapters we will be working with the normalized Landau-Lifshitz form, which can be written as

$$\frac{\mathrm{d}\hat{\mathbf{m}}}{\mathrm{d}t} = -\hat{\mathbf{m}}\times\mathbf{h}_{\text{eff}} - \alpha\hat{\mathbf{m}}\times\hat{\mathbf{m}}\times\mathbf{h}_{\text{eff}}. \tag{2.9}$$

Here $\hat{\mathbf{m}} = \mathbf{M}/M_s$ is the magnetization unit vector, the dimensionless field $\mathbf{h}_{\text{eff}}$ is defined as $\mathbf{h}_{\text{eff}} = \mathbf{H}_{\text{eff}}/H_k$ with the characteristic anisotropy field given by $H_k =$

11

$2K/\mu_0 M_s$, and the time is rescaled as

$$t \to t' = \frac{1}{1 - \alpha^2} \gamma H_k t.$$

Note that all the field related terms written in lowercase letters, if not specified, are dimensionless, i.e., are divided by H_k.

2.5 SPIN-TRANSFER TORQUES

Spin-transfer torque has been studies extensively ever since the publication of the paper by Slonczewski in 1996 [73]. In this paper Slonczewski describes a sandwich structure comprising two ferromagnetic layers, FM1 and FM2 from left to right, separated by a metallic nonmagnetic (NM) spacer. When a current flows from right to left, the conduction electrons, which flow from left to right, become polarised parallel to the magnetisation of FM1 when they go through it because of spin-dependent scattering taking place. The spin-polarised conduction electrons then drift through the NM spacer and reach the interface of FM2. The electrons are then partly reflected and partly transmitted at the interface. The spin of the transmitted electrons precess incoherently around the magnetisation of FM2. As a result, within a very short distance, the direction of spin-polarisation of the incoming electrons is re-oriented along the direction of the local magnetisation. This spin polarisation reorientation generates an incoming flow of angular momentum transmitted to the local magnetisation and exerts a torque on it. This torque is named by Slonczewski as spin-transfer torque and is given by [99]:

$$\tau = a\gamma \hat{\mathbf{m}} \times (\hat{\mathbf{m}} \times \hat{\mathbf{m}}_p) - b\gamma (\hat{\mathbf{m}} \times \hat{\mathbf{m}}_p), \tag{2.10}$$

where $\hat{\mathbf{m}}_p$ and $\hat{\mathbf{m}}$ are the magnetization unit vectors of the polarizer and the free layer. The first term is usually referred as the spin-torque term or Slonczewski term, the second is the effective field term. Both efficiency factors are proportional to

12
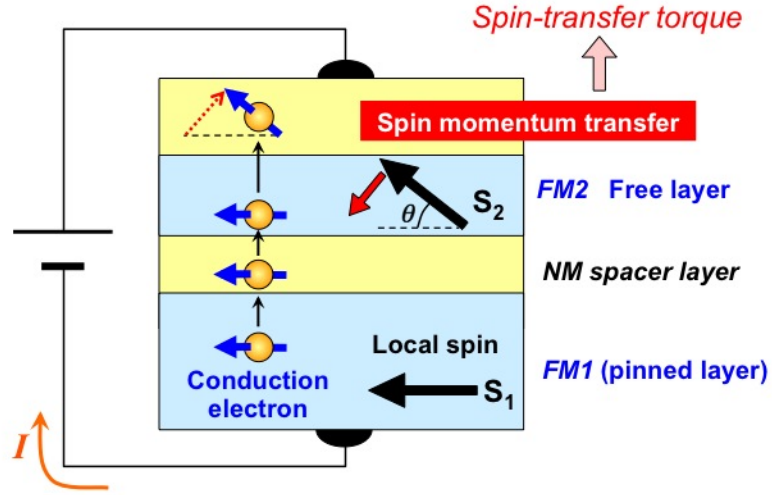
Figure 2.2: Illustration of spin-transfer torque in a spin valve device.

the current. Detailed theoretical quantum mechanical derivation of the spin transfer torque can be found in [99] and in [92].

For a GMR device of two ferromagnetic layers separated by a metal spacer, the perpendicular torque is negligible and the spin transfer torque is calculated using a simplified Boltzmann equation grafted with circuit theory [76, 92, 21, 52]

$$\tau_{\mathrm{st}} = g(\theta)\frac{\hbar}{2e}\frac{j}{d}\hat{\mathbf{m}} \times (\hat{\mathbf{m}} \times \hat{\mathbf{m}}_p), \tag{2.11}$$

where $g(\theta)$ is the spin-transfer efficiency function, θ is the angle between the two unit vectors $\cos\theta = \hat{\mathbf{m}} \cdot \hat{\mathbf{m}}_p$.

The efficiency function $g(\theta)$ is sometimes approximated by a constant, whereas the simplest functional form that incorporates the polarization P was found by Slonczweski in his original paper [73]

$$g(\theta) = \frac{1}{f(P)(3 + \cos\theta) - 4}, \tag{2.12}$$

13
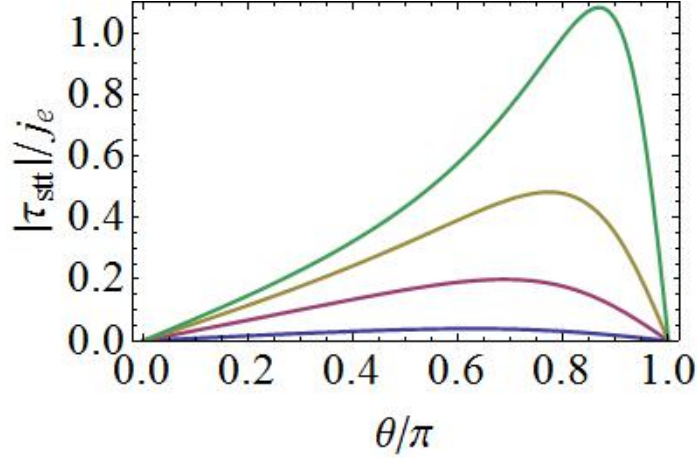
Figure 2.3: Dependence of spin transfer strength on the spin current polarization. The polarization coefficient P is set to 0.1, 0.3, 0.5 and 0.7 from bottom to top.

with

$$f(P) = \frac{(1+P)^3}{4P^{3/2}}. \tag{2.13}$$

The dependence of spin transfer strength on the spin polarization coefficient is plotted in Figure 2.3.

Building on his original work, Slonczewski applied an approximate form of magnetoelectronic circuit theory and derived a simple form in the symmetric case with equal ferromagnetic layer thicknesses, [76]

$$g(\theta) = \frac{q}{A + B\cos\theta}, \tag{2.14}$$

where q, A and B are determined by material and geometry. For a general spin-valve geometry, it should be replaced by [40, 92]

$$g(\theta) = \frac{q_+}{A + B\cos\theta} + \frac{q_-}{A - B\cos\theta}. \tag{2.15}$$

The LLG equation in the presence of spin-transfer torque, some times also referred as Landau-Lifshitz-Gilbert-Slonczewski (LLGS), is now written as

$$\frac{\mathrm{d}\hat{\mathbf{m}}}{\mathrm{d}t} = -\hat{\mathbf{m}} \times \mathbf{h}_{\text{eff}} + \alpha\hat{\mathbf{m}} \times \frac{\mathrm{d}\hat{\mathbf{m}}}{\mathrm{d}t} + \tau_{\text{st}}. \tag{2.16}$$

It should be pointed out that, in MTJs the effective field term can be of the order of 30% or more of the spin-torque term. This difference originates from the fact that

14

the spin transport in MTJ is mainly ballistic and there is no spin diffusive components involved. As a result, the precessional motion is more coherent when they enter the magnetic layer. This yields a larger amplitude of the effective field term. However, there is still no universal agreement in the quantitative dependence of the b term on the bias current [75, 66].

CHAPTER 3

SPIN TRANSFER INDUCED SWITCHING

The Stoner-Wohlfarth (SW) model of ferromagnetism [79] is the simplest model that is adequate enough to describe the physics of magnetization switching. In this chapter we first give a brief review on the field induced magnetic reversal on a SW nanomagnet, then we expend the existing model to include the spin-transfer torque and focus on spin-transfer induced switching.

3.1 STONER-WOHLFARTH MODEL

In the conventional case the nanomagnet possesses a uniaxial anisotropy, which is given by Eq. (2.5), and is subjected to an external magnetic field $\mathbf{H}$. Therefore, the total energy is the sum of the anisotropy energy E_{an} and the Zeeman energy $-\mathbf{M}\cdot\mathbf{H}$. Assuming the easy axis is along $\hat{\mathbf{z}}$, the free energy is given by

$$E = -\frac{KV}{M_s{}^2}(\mathbf{M}\cdot\hat{\mathbf{z}})^2 - \mu_0 V \mathbf{H}\cdot\mathbf{M}. \tag{3.1}$$

Examples of free energy with different external field strengths are shown in Figure 3.1. In the absence of an external field, the magnetization favors the two energy minimum states, $\hat{\mathbf{z}}$ and $-\hat{\mathbf{z}}$. The external field modifies the free energy and therefore shifts the energy minima. In a quasi-static process, the magnetization vector $\mathbf{M}$ always follows the motion of one of the minima until it loses its stability. Then $\mathbf{M}$ is subject to a jump towards the other minimum.

The minimum condition at θ_0 satisfies

$$\left(\frac{\partial E}{\partial \theta}\right)_{\theta=\theta_0} = 0, \quad \left(\frac{\partial^2 E}{\partial^2 \theta}\right)_{\theta=\theta_0} > 0. \tag{3.2}$$

16
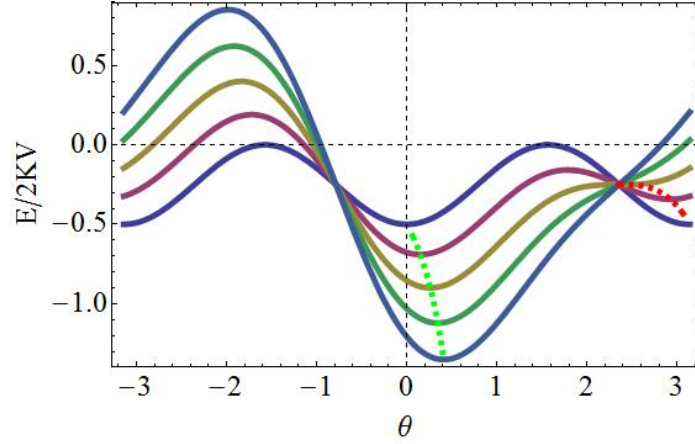
Figure 3.1: Free energy of a SW nanomagnet. The external field is applied at $\theta = \pi/4$ with its magnitude varying from 0 to H_k. The green and red dashed lines represent the trajectory of two energy minima as functions of the magnitude of external field.

The switching condition above leads to a critical switching field which can be expressed in terms of the following parametric form, known as Stoner-Wohlfarth Astroid (see Figure 3.3)

$$
\begin{cases}
\dfrac{H_\perp}{H_k} = \pm \sin^3 \theta, \\[2ex]
\dfrac{H_z}{H_k} = - \cos^3 \theta.
\end{cases}
\tag{3.3}
$$

where the characteristic anisotropy field H_k is given by $H_k = 2K/\mu_0 M_s$.

A geometrical approach which generalizes the construction of critical switching fields for any arbitrary anisotropy was proposed by A. Thiaville in 2000 [83]. In his approach the three-dimensional critical fields, which are called as critical surfaces, are calculated by using the critical condition of energy extrema on a magnetization unit sphere. Consequently, this method can only be applied to the magnetic systems with well defined free energies in which the equilibrium states are always located at the energy extrema.

When a nonconservative field, such as the spin-transfer toque, is applied, it pushes the magnetization stable state away from an energy minimum, some times even towards an maximum. Generally speaking, the equilibria are no longer associated with the energy extrema, and therefore the geometrical method is no longer valid. In the

17
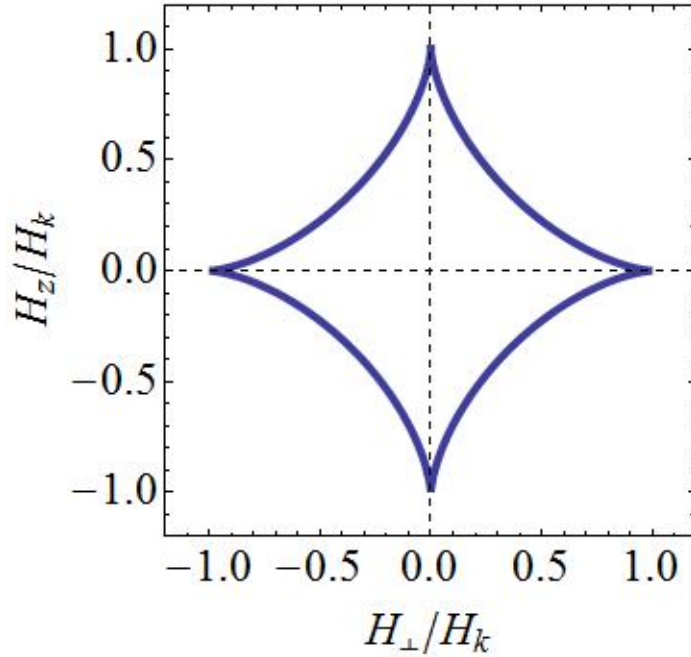
Figure 3.2: Stoner-Wohlfarth Astroid. Figure from [79].

following sections we describe a more general approach which is derived directly from the LLG equation and takes into account both the conservative forces and nonconservative forces, and then we apply it to different magnetic systems in the presence of both external fields and spin-transfer toques.

3.2 CLASSIFICATION OF EQUILIBRIA

Before digging into the details of magnetic systems, we first summarize the types of equilibrium in a two-dimensional dynamical planar system in general. For a nonlinear dynamical system such as the magnetic system which is modeled by the LLG equation, we can determine the asymptotic behaviors of solutions near equilibrium points by linearizing the equation. A complete study of such systems can be found in Ref. [28].

Consider a planar linear system of the form $\dot{\mathbf{X}} = A\mathbf{X}$, where $\mathbf{X} = \{x_1, x_2\}$ is the coordinate vector and A is the 2×2 coefficient matrix. When A is time independent, given its eigenvalues $\mu_{1,2}$ and associated eigenvectors $\mathbf{V}_1$ and $\mathbf{V}_2$, the general solution

18

can be written as

$$\mathbf{X}(t) = c_1 e^{\mu_1 t}\mathbf{V}_1 + c_2 e^{\mu_2 t}\mathbf{V}_2, \tag{3.4}$$

where coefficients c_1 and c_2 are determined by the initial condition. Note that the origin is always an equilibrium point for such system.

Since the eigenvalues satisfy

$$\mu^2 - (\mathrm{tr}A)\mu + \det A = 0, \tag{3.5}$$

they can be written as functions of $\mathrm{tr}A$ and $\det A$

$$\mu_{1,2} = \frac{1}{2}\left(\mathrm{tr}A \pm \sqrt{(\mathrm{tr}A)^2 - 4\det A}\right). \tag{3.6}$$

Therefore knowing $\mathrm{tr}A$ and $\det A$ gives the eigenvalues of A and virtually everything about the geometry of its solutions. From Eq. (3.6) we can see that the sign of $(\mathrm{tr}A)^2 - 4\det A$ separates the eigenvalues into two regions on the trace-determinant plane with real and complex values:

1. Complex with nonzero imaginary part if $(\mathrm{tr}A)^2 - 4\det A < 0$;

2. Real and distinct if $(\mathrm{tr}A)^2 - 4\det A > 0$;

3. Real and repeated if $(\mathrm{tr}A)^2 - 4\det A = 0$.

According to Eq. (3.4), the types of equilibrium are determined by its eigenvalues. In terms of phase portraits, if $(\mathrm{tr}A)^2 - 4\det A < 0$, then the real part of the eigenvalues is $(\mathrm{tr}A)/2$, and we have

1. Spiral sink if $\mathrm{tr}A < 0$;

2. Spiral source if $\mathrm{tr}A > 0$;

3. Center if $\mathrm{tr}A = 0$.

If $(\mathrm{tr}A)^2 - 4\det A > 0$, both eigenvalues are real, and we have

1. Real sink if $\det A > 0$ and $\mathrm{tr}A < 0$;

2. Real source if $\det A > 0$ and $\mathrm{tr}A > 0$;

3. Saddle point if $\det A < 0$.

19
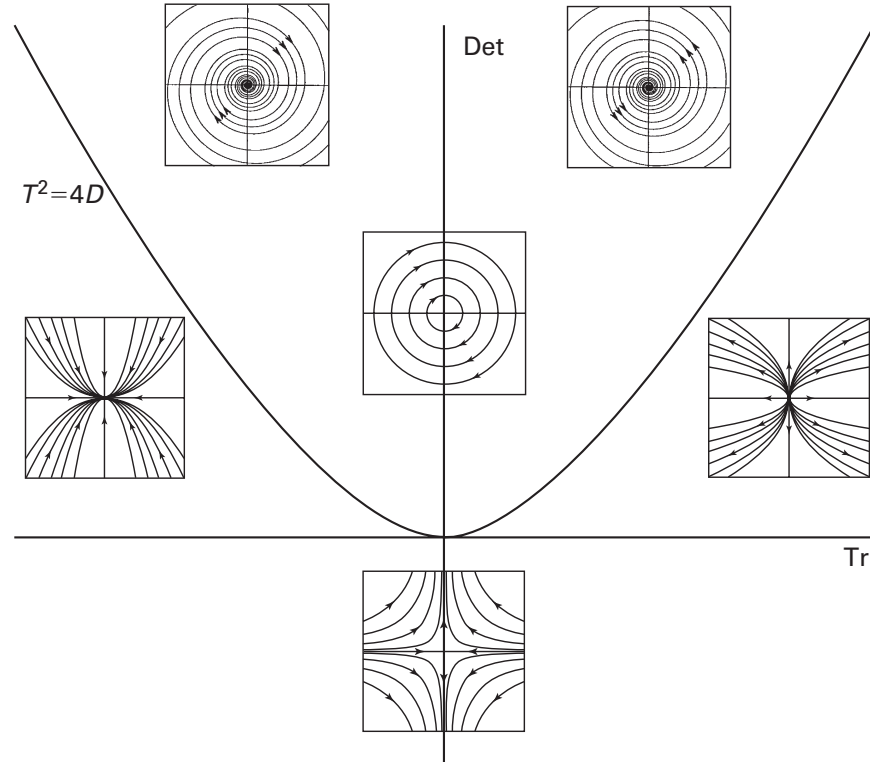
Figure 3.3: Phase portraits of different types of equilibrium in the trace-determinant plane. The parabola represents $(\text{tr}A)^2 - 4\det A = 0$. Diagram from Ref. [28].

The simple analysis already provides enough information to describe the asymptotic behavior of a solution in general. Fig. 3.3 illustrates the phase portraits of different types of equilibrium in the trace-determinant plane. For any linear planar system, the solutions near the origin can always be classified as one of the six phase portraits by using a proper linear transformation matrix.

It's often impossible to write down explicit solutions of nonlinear differential equations, such as the LLG equation. However, one exception occurs when we have equilibrium solutions. If the equilibrium states in a magnetic system can be found, then by linearizing the LLG equation near the equilibria, the solutions should resemble those portraits in the linearized systems. The detailed procedures will be discussed in the next section.

20

3.3 Critical surfaces

In this section we derive the general formula for the critical surface using the normalized form of LLG equation. As we discussed in the previous chapter, the spin-transfer torque (2.11) should be included in the LLG equation to describe the spin-transfer effect in a GMR device, which leads to the LLGS equation of the form (2.16). Alternatively, we could also stick to the normalized LLG equation (2.9) by adding a spin-transfer field into the effective field as

$$\mathbf{h}_{\text{eff}} = \mathbf{h} + \mathbf{h}_{\text{an}} + \mathbf{h}_{\text{st}}, \tag{3.7}$$

where the spin-transfer field is determined by equation

$$\boldsymbol{\tau}_{\text{st}} = \hat{\mathbf{m}} \times \mathbf{h}_{\text{st}}. \tag{3.8}$$

An equilibrium of Eq. (2.9) can be found when the condition $\hat{\mathbf{m}} \times \mathbf{h}_{\text{eff}} = 0$ is satisfied, which indicates that the magnetization at equilibrium should be parallel to the total effective field. This is equivalent to

$$\mathbf{h}_{\text{eff}} = \lambda \hat{\mathbf{m}}_0, \tag{3.9}$$

where λ is a parameter that describes a set of external fields satisfying the equilibrium condition for $\hat{\mathbf{m}}_0$. We will use the subscript "0" to denote an equilibrium state hereafter. The stability of an equilibrium can be analyzed by linear expansion of Eq. (2.9) with $\hat{\mathbf{m}} = \hat{\mathbf{m}}_0 + \delta\hat{\mathbf{m}}$. In spherical coordinates with three orthogonal unit vectors defined as

$$\hat{\mathbf{m}} = \sin\theta\cos\phi\hat{\mathbf{x}} + \sin\theta\sin\phi\hat{\mathbf{y}} + \cos\theta\hat{\mathbf{z}}, \tag{3.10a}$$

$$\hat{\theta} = \frac{\partial\hat{\mathbf{m}}}{\partial\theta} = \cos\theta\cos\phi\hat{\mathbf{x}} + \cos\theta\sin\phi\hat{\mathbf{y}} - \sin\theta\hat{\mathbf{z}}, \tag{3.10b}$$

$$\hat{\phi} = \frac{1}{\sin\theta}\frac{\partial\hat{\mathbf{m}}}{\partial\phi} = -\sin\phi\hat{\mathbf{x}} + \cos\phi\hat{\mathbf{y}}, \tag{3.10c}$$

21

the expansion can be expressed in terms of two coupled linear differential equations in the matrix form

$$
\begin{pmatrix} \dot{\delta\theta} \\ \sin\theta_0 \dot{\delta\phi} \end{pmatrix} = A\left(\theta_0, \phi_0\right) \begin{pmatrix} \delta\theta \\ \sin\theta_0 \delta\phi \end{pmatrix},
\tag{3.11}
$$

The equation describes a planar linear system with coefficient matrix $A(\theta_0, \phi_0)$ given by

$$
A = \begin{pmatrix} \partial_\theta(\alpha h^\theta_{\text{eff}} + h^\phi_{\text{eff}}) & \frac{1}{\sin\theta}\partial_\phi(\alpha h^\theta_{\text{eff}} + h^\phi_{\text{eff}}) \\ \partial_\theta(\alpha h^\phi_{\text{eff}} - h^\theta_{\text{eff}}) & \frac{1}{\sin\theta}\partial_\phi(\alpha h^\phi_{\text{eff}} - h^\theta_{\text{eff}}) \end{pmatrix}.
\tag{3.12}
$$

Here the abbreviated notations ∂_θ and ∂_ϕ stand for $\partial/\partial\theta$ and $\partial/\partial\phi$, resectively, and the superscripts θ and ϕ indicate the corresponding component of a vector field (e.g., $h^\theta_{\text{eff}} = \mathbf{h}_{\text{eff}} \cdot \hat{\theta}$, etc.).

According to the discussion in Sec. 3.2, the different types of stationary solutions can be classified by the eigenvalues $\mu_\pm$ of the matrix A, which are uniquely determined by its determinant $\det A$ and trace $\text{tr}A$. Particularly, when an equilibrium is stable, both eigenvalues $\mu_\pm$ are either complex conjugates with negative real parts, or are negative real numbers, which lead to the stability criterion:

$$
\det A > 0 \text{ and } \text{tr}A < 0.
\tag{3.13}
$$

In order to calculate the stability criterion, we need to write the total effective field $\mathbf{h}_{\text{eff}}$ explicitly. Generally speaking, it can be written as $\mathbf{h}_{\text{eff}} = \mathbf{h} - \nabla\varepsilon + \mathbf{h}_{\text{st}}$, where $\mathbf{h}$ is the external field, ε is the anisotropy energy, and $\mathbf{h}_{\text{st}}$ is the spin effective field which is usually a nonconservative vector field. When the system is at equilibrium, the external field can be expressed in spherical coordinates as

$$
\mathbf{h} = \lambda\hat{\mathbf{m}}_0 + \left(\partial_\theta\varepsilon - h^\theta_{\text{st}}\right)_0 \hat{\theta}_0 + \left(\frac{1}{\sin\theta}\partial_\phi\varepsilon - h^\phi_{\text{st}}\right)_0 \hat{\phi}_0.
\tag{3.14}
$$

The right hand side of Eq. (3.14) maps an equilibrium $\hat{\mathbf{m}}_0$ in parameter space $\{\lambda, \theta_0, \phi_0\}$ to the corresponding external field $\mathbf{h}$ in field space $\{h_x, h_y, h_z\}$. According to Poincaré-Hopf theorem, there are at least two sink or source type equilibrium states existing on the unit sphere of magnetization for any smoothly varying field.

22

By substituting Eq. (3.14) into the matrix A (Eq. (3.12)), one finds that $\mathrm{tr}A$ is linear in λ with a negative coefficient, and $\det A$ is a quadratic function of λ with a positive quadratic coefficient. To simplify the expressions, we introduce a vector field $\mathbf{f} = -\nabla\varepsilon + \mathbf{h}_{\mathrm{st}}$ and its gradient

$$\nabla\mathbf{f} = \begin{pmatrix} \partial_\theta f^\theta & \partial_\theta f^\phi \\ \partial_\phi f^\theta & \partial_\phi f^\phi \end{pmatrix}, \tag{3.15}$$

with each of the components given by

$$\partial_\theta f^\theta = -\partial_{\theta\theta}\varepsilon + \partial_\theta h_{\mathrm{st}}{}^\theta, \tag{3.16a}$$

$$\partial_\theta f^\phi = -\partial_\theta\left(\frac{1}{\sin\theta}\partial_\phi\varepsilon\right) + \partial_\theta h_{\mathrm{st}}{}^\phi, \tag{3.16b}$$

$$\partial_\phi f^\theta = \frac{\cos\theta}{\sin\theta}\left(\frac{1}{\sin\theta}\partial_\phi\varepsilon - h_{\mathrm{st}}{}^\phi\right) - \frac{1}{\sin\theta}\left(\partial_{\theta\phi}^2\varepsilon - \partial_\phi h_{\mathrm{st}}{}^\theta\right), \tag{3.16c}$$

$$\partial_\phi f^\phi = -\frac{\cos\theta}{\sin\theta}\left(\partial_\theta\varepsilon - h_{\mathrm{st}}{}^\theta\right) - \frac{1}{\sin^2\theta}\partial_{\phi\phi}^2\varepsilon + \frac{1}{\sin\theta}\partial_\phi h_{\mathrm{st}}{}^\phi. \tag{3.16d}$$

The roots of equations $\mathrm{tr}A = 0$ and $\det A = 0$ can then be expressed in terms of the partial derivatives of f as

$$\lambda_{\mathrm{T}} = \frac{1}{2}\left[\partial_\theta f^\theta + \partial_\phi f^\phi + \frac{1}{\alpha}\left(\partial_\theta f^\phi - \partial_\phi f^\theta\right)\right], \tag{3.17}$$

and

$$\lambda_\pm = \frac{\partial_\theta f^\theta + \partial_\phi f^\phi}{2} \pm \sqrt{\left(\frac{\partial_\theta f^\theta - \partial_\phi f^\phi}{2}\right)^2 + \partial_\theta f^\phi \partial_\phi f^\theta}. \tag{3.18}$$

In terms of the critical values λ_{T} and $\lambda_\pm$, the stability criterion (3.13) becomes

$$\begin{cases} \lambda > \mathrm{Max}(\lambda_{\mathrm{T}}, \lambda_+) & \text{if } \lambda_{\mathrm{T}} \geqslant \lambda_-, \\ \lambda_{\mathrm{T}} < \lambda < \lambda_- & \text{if } \lambda_{\mathrm{T}} < \lambda_-. \end{cases} \tag{3.19}$$

When $\lambda_\pm$ are complex, $\det A$ is always positive and criterion (3.19) can be further simplified as $\lambda > \lambda_{\mathrm{T}}$.

The criterion above only addresses the stable and unstable equilibra. From the geometry point of view, it is equally important to distinguish the two types of unstable equilibria, i.e., source and saddle, which requires the complete classification of equilibrium types. Such a complete classification is given in Appendix A.

23

Substituting λ_+, λ_- and λ_T for λ into Eq. (3.14) generates three surfaces in the three-dimensional field space, which we denote by S_+, S_- and S_T respectively

$$S_T(\theta, \phi, j) = \mathbf{h}(\lambda_T(\hat{\mathbf{m}}, j), \hat{\mathbf{m}}, j), \qquad (3.20)$$

and

$$S_\pm(\theta, \phi, j) = \mathbf{h}(\lambda_\pm(\hat{\mathbf{m}}, j), \hat{\mathbf{m}}, j). \qquad (3.21)$$

By varying the unit vector $\hat{\mathbf{m}}$ all over the 4π solid angle, the expressions above give three closed surfaces in the three-dimensional field space. It should be noted that, θ and ϕ are two angle coordinates of the magnetization unit vector $\hat{\mathbf{m}}$. Since $\hat{\mathbf{m}}$ does not always lie in the same plane with the external field $\mathbf{h}$ in the general cases, when plotting the critical surfaces, one need to decompose the field into Cartesian coordinates and use the parametric form of each component instead of simply varying the angles on the magnetization unit sphere surface.

The physical meaning of the three surfaces is that: when the external field crosses S_T, one of the equilibria changes its stability, e.g., from a source to a sink or vice versa (it cannot become a saddle); when it crosses $S_\pm$, one sink or source merges with a saddle point. This process could be a destruction or a creation with the two equilibra involved (one of which must be a saddle), depending on the direction that the field crosses the $S_\pm$ surface. Therefore there is always at least one equilibrium changes its stability when the external field crosses any one of the surfaces. Since only the distabilizing of a stable equilibrium is physically significant, the entire critical surface should be only constructed by using the parts of the three surfaces that satisfy stability criterion (3.19). The procedure will be illustrated in the following chapters in the cases of spin valve and SHE device.

The approach described in this section can be used to find the switching phase diagrams for any magnetic nonlinear systems in the presence of spin-polarized currents, provided that the macrospin approximation is valid. In addition, since different types

24

of boundaries correspond to different distabilizing processes, it is possible to get an intuitive picture of switching by analyzing the critical surfaces instead of solving the LLG equation directly.

CHAPTER 4

APPLICATION IN SPIN VALVES

4.1 SPIN VALVES WITH PERPENDICULAR ANISOTROPY

We consider a spin valve nanopillar with both the free layer and fixed layer (polarizer) having perpendicular-to-plane uniaxial anisotropy. The magnetization direction of the reference layer is pointing towards the $+\hat{\mathbf{z}}$ direction. For a positive current, the electrons flow upwards. The spin valve and the associated spherical coordinates are shown in figure 4.1.
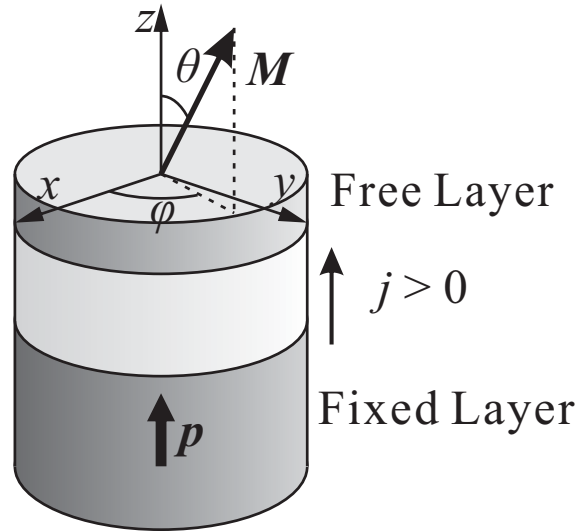
Figure 4.1: Schematics of a spin valve nanopillar with a perpendicular polarizer $\hat{\mathbf{p}}$. Both the easy axis of the free layer and the polarizer are pointing along the z axis. For a positive current, the electrons flow from the fixed layer to the free layer.

In our following calculation of the spin valve nanopillar, we adopt the Slonczewski spin-transfer torque of the form (2.11), then the equivalent effective field can be

written as

$$
\begin{aligned}
\mathbf{H}_{\mathrm{st}} &= \frac{1}{\mu_0 M_{\mathrm{s}}} \frac{I}{Ae} \frac{\hbar}{2} \frac{1}{d} g(\hat{\mathbf{m}} \cdot \hat{\mathbf{p}})(\hat{\mathbf{m}} \times \hat{\mathbf{p}}) \\
&= -\frac{1}{\mu_0 M_{\mathrm{s}}} \frac{I}{Ae} \frac{\hbar}{2} \frac{1}{d} g(\cos\theta) \sin\theta \hat{\phi}.
\end{aligned}
\tag{4.1}
$$

Here $I/Ae = j/e$ is the particle current density of itinerant electrons with A being the cross-section area of the device and j being the electric current density, d is the thickness of the free layer. We adopt Eq. (2.12) for the spin-torque efficiency function $g(\theta)$. The spin polarization of the electrons is set to $P = 50\%$ in all calculations.

4.2 Critical surfaces of the spin valve nanopillar

Assuming the free layer has perpendicular uniaxial magnetization anisotropy, the rescaled dimensionless anisotropy energy is written as

$$
\varepsilon = \frac{E_{\mathrm{an}}}{2KV} = -\frac{1}{2}\cos^2\theta,
\tag{4.2}
$$

Since the direction of polarization is collinear with the easy-axis of the reference layer, the spin-transfer torque field in this geometry is rotationally symmetric with respect to $\hat{\mathbf{z}}$. The dimensionless form is written as

$$
\frac{\mathbf{H}_{\mathrm{st}}}{H_{\mathrm{k}}} = h_{\mathrm{st}}^{\phi}(\theta) \ \hat{\phi},
\tag{4.3}
$$

with its magnitude given by

$$
h_{\mathrm{st}}^{\phi}(\theta) = -\frac{j}{j_0} g(\cos\theta) \sin\theta,
\tag{4.4}
$$

where the characteristic current density is defined as $j_0 = 4edK/\hbar$. The spin torque term is proportional to the current density and vanishes at $j = 0$.

Substituting ε from Eq. (4.2) and h_{st} from Eq. (4.3) into Eq. (3.17) and Eq. (3.18) we get the expressions of the critical values of λ for the spin valve

$$
\lambda_{\mathrm{T}} = \frac{1}{2}\sin^2\theta - \cos^2\theta + \frac{1}{2\alpha}\left(\frac{\cos\theta}{\sin\theta}h_{\mathrm{st}} + \frac{\partial h_{\mathrm{st}}}{\partial\theta}\right),
\tag{4.5}
$$

27

and

$$\lambda_{\pm} = \frac{1}{2}\sin^2\theta - \cos^2\theta \pm \sqrt{\frac{1}{4}\sin^4\theta - \frac{\cos\theta}{\sin\theta}h_{\text{st}}\frac{\partial h_{\text{st}}}{\partial \theta}}. \qquad (4.6)$$

Note that the current-dependent term in the expression (4.5) comes with a factor of $1/\alpha$. Since Gilbert damping is usually small, this means that λ_{T} is very sensitive to the changes of the current. The current contribution to Eq. (4.6), does not contain a similar large factor, thus $\lambda_{\pm}$ are relatively insensitive to the current changes. Since the expressions are only functions of θ, we can plot them in a two-dimensional λ-θ plane. Figure 4.2 shows the critical values of λ as functions of θ with (bottom panel) and without (top panel) the spin transfer torque.

Next we calculate the critical surfaces using the critical values of λ we just derived. The independence of angle ϕ on ε and h_{st}^{ϕ} simplifies Eq. (3.14) as

$$\mathbf{h} = \lambda\hat{\mathbf{m}} + (\sin\theta\cos\theta)\hat{\theta} - h_{\text{st}}^{\phi}\hat{\phi}, \qquad (4.7)$$

which leads to the rotational symmetry in the resulting critical surfaces. It should be noted that since the angle variables θ and ϕ in this expression refer to the direction of the magnetization instead of the direction of the external magnetic field. In order to plot the critical field surfaces, we need to decompose the field expression (4.7) into Cartesian coordinates as

$$h_x = (\lambda + \cos^2\theta)\sin\theta\cos\phi - h_{\text{st}}^{\phi}\sin\phi, \qquad (4.8\text{a})$$

$$h_y = (\lambda + \cos^2\theta)\sin\theta\sin\phi + h_{\text{st}}^{\phi}\cos\phi, \qquad (4.8\text{b})$$

$$h_z = (\lambda - \sin^2\theta)\cos\theta. \qquad (4.8\text{c})$$

Because of the symmetry, we can instead plot the critical surfaces on a two-dimensional field plane. By introducing the perpendicular component of the external field

$$h_{\perp} = \sqrt{h_x^2 + h_y^2} = \sqrt{(\lambda + \cos^2\theta)^2\sin^2\theta + (h_{\text{st}}^{\phi})^2}, \qquad (4.9)$$

which is only a function of θ, the critical surfaces now reduces to two-dimensional critical curves, as shown in Fig. 4.3. When the field crosses those curves from inside,

28
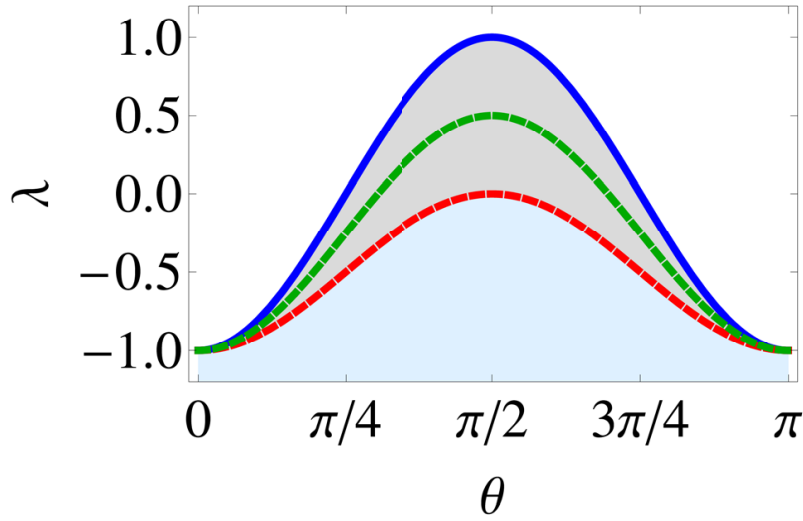
(a)
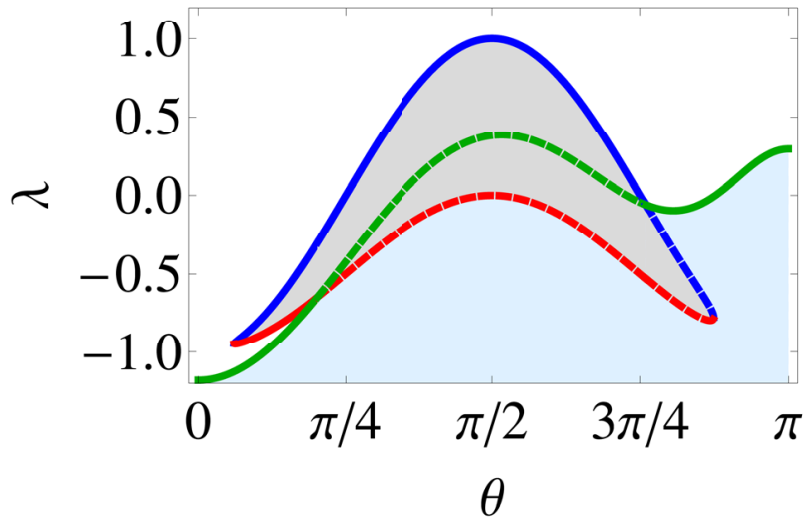
(b)

Figure 4.2: Critical values of λ. The current densities are (a) $j/j_0 = 0$, and (b) $j/j_0 = 0.1$. The blue, red and green curves denote λ_+, λ_- and λ_{T}, respectively. The stable (white) region and unstable (gray) region are separated by solid lines. The spin polarization $P = 50\%$ and the damping parameter $\alpha = 0.1$ are adopted in all figures.

29

one of the stable equilibrium either is destabilized by the spin-transfer torque or merges with a saddle point, as discussed in the previous section.

4.3 ANALYSIS OF EQUILIBRIA AND DESTABILIZATION MODES

Conventional astroid

We first analyze the case with $j = 0$, which should reproduce the conventional SW astroid. In the λ-θ plane, the $\lambda_{\pm}$ curves form a closed region with λ_{T} being the midline. They separate the entire plane into three parts, which can be classified, according to criterion (3.19), as sink, saddle, and source as shown in Figure 4.2(a) from top to bottom. Since saddle and source are both unstable, the stable (sink) region and the unstable (saddle and source) region are separated by λ_+ only. This separation gives the critical curve S_+ in the field plane, which reproduces the conventional SW astroid. In addition, there are also two more curves, S_- and S_{T}, inside the astroid as shown in Figure 4.3(a). Just as expected, neither S_- nor S_{T} is critical in this case.

The equilibria and destabilization mode in this case are well understood. There are four equilibria (two minima, one maximum and one saddle point) when the field is inside the astroid. In terms of the language in the classification of planar systems, they are sink, source and saddle point, respectively. When the field crosses the boundary of the astroid which is solely given by S_+, one of the minima merges with the saddle point. If the magnetization happens to be at the destabilizing minimum, it will be switched to the other minimum when the field moves outside the astroid.

The destabilization is even more straightforward in the λ-θ representation by mapping the field to the equilibria. A field vector that is inside the astroid maps four points into the λ-θ plane, each of which corresponds to one of its equilibria and is labeled by angle θ and λ. The value of λ characterizes the stability of the equilibrium. When merging happens, the saddle point collides with one of the sinks at a point on
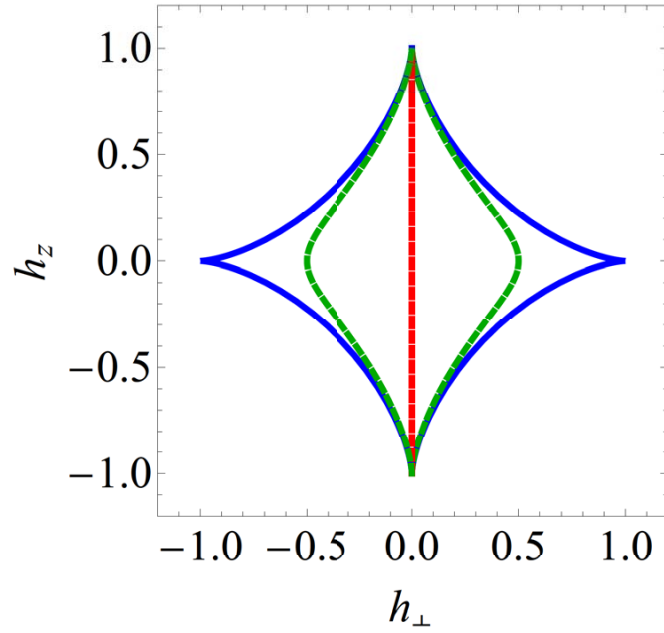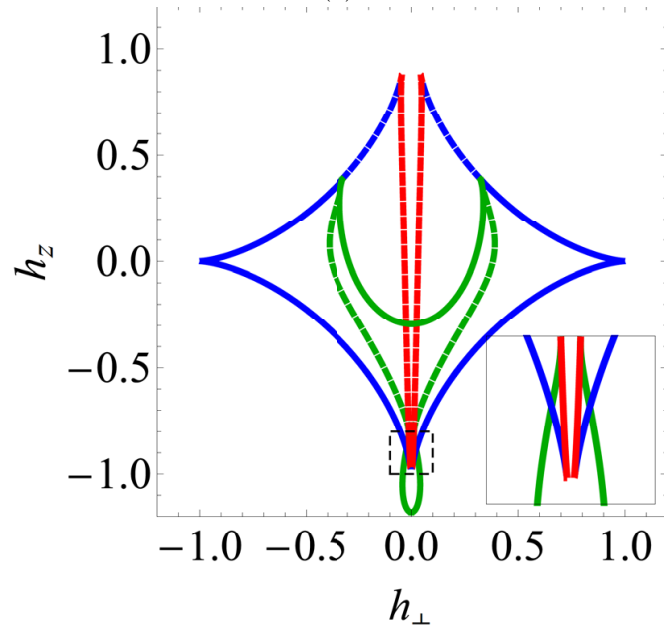
Figure 4.3: Critical surfaces in the field plane. The current densities are (a) $j/j_0 = 0$, and (b) $j/j_0 = 0.1$. The same color scheme is used for S_+, S_- and S_T. The critical curve (solid lines) corresponds to the solid parts of the critical λ curves which compose the boundary of the stable region in Fig. 4.2.

λ_+. The merging between the saddle point and the source, which should happen on λ_-, is not so obvious in this case because instead of forming a volume, S_- degenerates into a line along the z axis and hence it is not able to define a similar crossing process. λ_{T} always lies between $\lambda_\pm$, where $\det A < 0$, and therefore does not affect the stability of either a sink or a source.

In a more general case, however, all the three critical curves may be active in destabilizing a sink. This will be discussed in the following case when spin-transfer torque is available.

Modified astroid

In the presence of spin-transfer torque, the equilibria exhibit two major differences from the conventional ones.

First, according to Eq. (3.14) the equilibrium $\hat{\mathbf{m}}$ is no longer located in the same field plane. The consequence is that the classification of equilibria by energy extremum is not appropriate, and therefore we should adopt the more general descriptions, i.e., sink, saddle and source. Nevertheless, because of the rotational symmetry, the azimuthal angle ϕ of an equilibrium is uniquely determined by its polar angle θ and λ by

$$\tan \phi = \frac{h_{\mathrm{st}}}{(\lambda + \cos^2 \theta) \sin \theta}. \tag{4.10}$$

Therefore the λ-θ plane still provides enough information in describing the destabilization of equilibra. Similarly, the switching phase diagram can still be represented by the critical curve.

Second, the boundary that separates stable and unstable regions in the λ-θ plane is composed of the line segments of $\lambda_\pm$ and λ_{T}, and so is the critical surface. This is purely a spin-transfer effect, which leads to more destabilization modes than the conventional case.

32

The stability in each region in the λ-θ plane is determined by criterion (3.19). We take $j/j_0 = 0.1$ as an example. Figure 4.2(b) shows the stable and unstable regions as well as the separating boundary (solid lines) in the λ-θ plane. By mapping the lines into the field plane, we get a modified astroid as shown in Figure 4.3(b). The modifications mainly come from two aspects: (1) the $\lambda_\pm$ region does not cover the ranges of both small and large θ, which leaves a hollow, surrounded by S_-, along the direction of easy axis inside the astroid; (2) two segments of the λ_T line compose both ends of the boundary in the λ-θ plane and modify the astroid with a "depression" at the top and a "bubble" at the bottom. The three-dimensional critical surfaces in field plane with current being the third dimension is plotted in Figure 4.4, which well reflects the trend of modifications.

Similar to the conventional case, there are four equilibria for the field inside the region enclosed by $S_\pm$. When the field crosses the boundary, either through S_+ or through S_-, the saddle point collides with a sink or a source, which reduces the number of equilibria to two. In the λ-θ plane, λ_T destabilizes a sink to a source at the line segments outside the $\lambda_\pm$ regions but keeps the number of total equilibria the same. This is usually referred as local destabilization. In terms of the number of sinks, the modified astroid encloses a region with two or more stable equilibria, although the total number of equilibria inside could be two or four. Whenever the external field crosses the solid line from inside, one of the sink loses its stability by either merging with a saddle (through $S_\pm$) or locally destabilizing (through S_T). The latter is purely a spin-transfer effect. The destabilization modes are illustrated in Figure 4.5. A graphic method for plotting the equilibra in the λ-θ plane is given in details in Appendix B. This method describes an simple but intuitive way to track the equilibria with varying parameters, such as the external field and the current density.

Note that there is a small triangular region enclosed by $S_\pm$ and S_T at the bot-
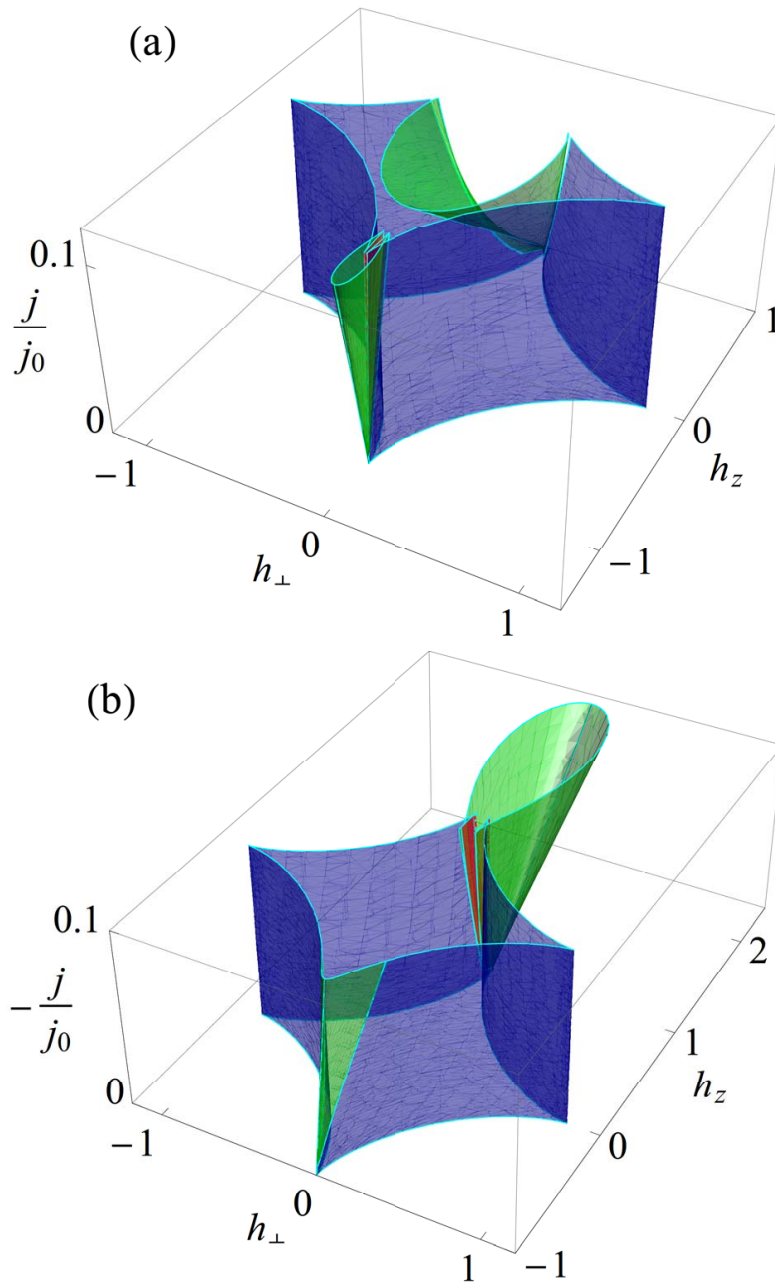
Figure 4.4: 3D critical surfaces in the $\{h_\perp, h_z, j\}$ current-field space. (a), $j/j_0 > 0$; (b), $j/j_0 < 0$. The asymmetry of the two sub-figures is due to the asymmetry of the efficiency factor $g(\cos\theta)$.
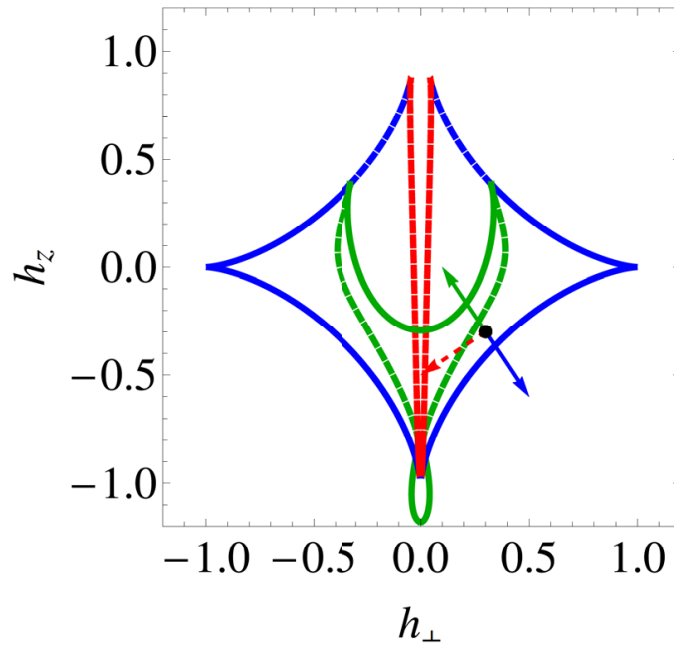
(a)
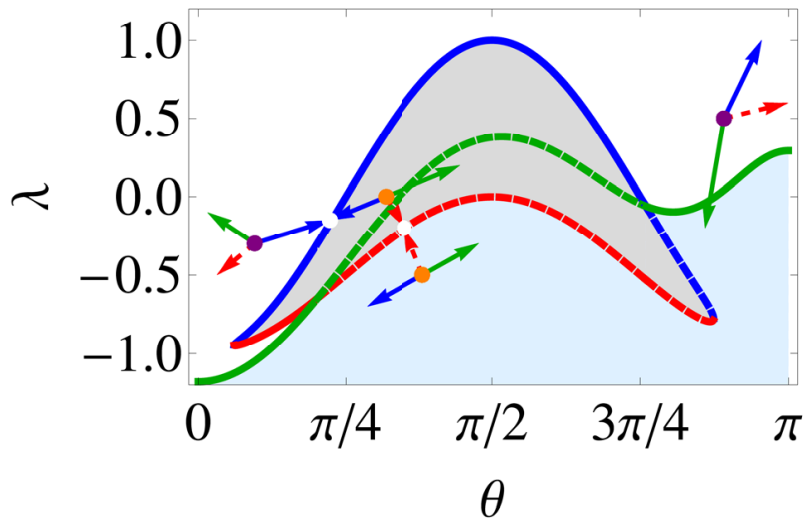
(b)

Figure 4.5: Illustration of different destabilization modes. (a), the external field is shown by the black dot, the blue, red, and green arrow indicate the different paths of the field, which cross the S_+, S_- and S_T, respectively. (b), the four equilibria of the field are marked in purple(stable) and orange(unstable), the arrows indicate the routes of the equilibria when the field changes, the white dots indicate merging of two equilibria.

tleneck which, according to our discussion, should have three sinks and a saddle but no source. When the field moves out of this region, however, it destabilizes one of the sinks, depending on which boundary it crosses. An intuitive way to understand it can be done by adding λ as the third dimension in the field plane. Because each equilibrium is associated with a value of λ. When the external field changes, it varies smoothly until merging takes place. We therefore can plot λ as a function of the field instead of the angles. The function $\lambda(\mathbf{h})$ is now a folded surface in three-dimensional λ-$\mathbf{h}$ space, indicating that a single point in the field plane corresponds to multiple λ values, as shown in Figure 4.6. By crossing different boundaries of the triangle, different sink is destabilized. The two trajectories in Figure 4.6 show how an sink, initially at the center, becomes unstable through the triangle region: (1) directly get into the triangular region and merges with a saddle point at S_+, and (2) get into the bubble region at the bottom through the "tunnel" enclosed by S_- and go back into the triangular region via S_+, then destabilize either at S_- by merging or at S_T by local destabilization.

4.4 Switching diagrams in a slightly misaligned axial field

The switching phase diagram in the same geometry with the field applied strictly along the direction of easy axis has been calculated in the literature by different methods [7, 50, 101]. The two stable states in this case are often referred as parallel (P, low resistance) state and antiparallel (AP, high resistance) state, which are located at the north and south poles, respectively.

The P to AP and AP to P switchings in the phase diagram correspond to two lines with different slopes. In term of the critical surfaces, they are determined by S_T

36
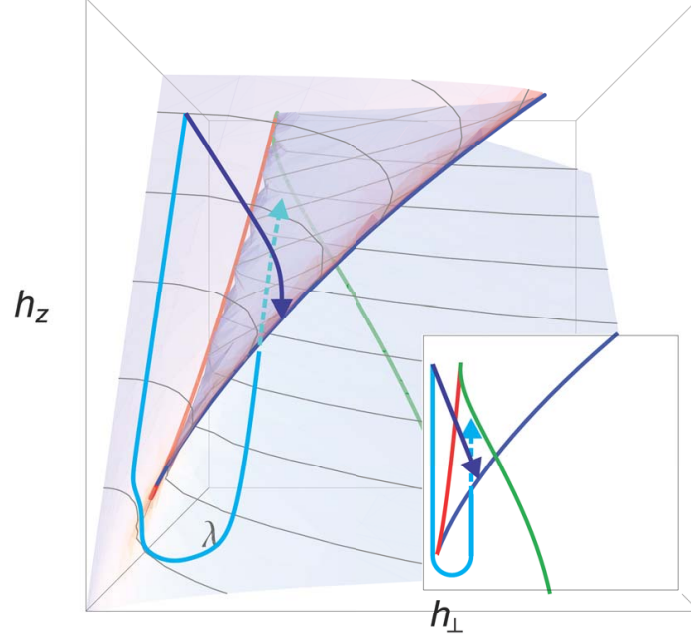
Figure 4.6: 3D illustration of the two destabilization modes through different trajectories in the triangular region near the bottom of the modified astroid. Only right part is shown in the field plane.

at $\theta = 0$ and $\theta = 0$, respectively

$$\left(\frac{j}{j_0}\right)_{P \to AP} = -\frac{\alpha}{g(0)}(H + H_\mathrm{k}), \tag{4.11a}$$

$$\left(\frac{j}{j_0}\right)_{AP \to P} = -\frac{\alpha}{g(\pi)}(H - H_\mathrm{k}). \tag{4.11b}$$

Such a diagram has been studied extensively in experiment for various multilayer spin valves with perpendicular anisotropy [50, 51, 85, 42]. The switching boundaries determined by the switching fields and currents evolve linearly over a large range. However, a strong deviation, refered as canted states in Ref. [50], occurs near the zero-current switching fields (see Figure 3 in Ref. [50], Figure 2 in Ref. [51], and Figure 3 in Ref. [85]). Experimentally it seems that the switching fields at zero current act as two barriers which require much bigger current to overcome. The AP/P coexisting region continues for larger field when bigger current is applied (for example, the top left corner in Figure 3 in Ref. [50]). This experimental discrepancy with theoretical prediction was investigated by J. Cucchiara, et al. in Ref. [17] in

37

terms of the picture of energy dissipation, and by S. Le Gall, et al. in Ref. [42] using the approximated two-dimensional model. Both analysis deduce that the uniaxial symmetry breaking causes the experimental results.

There are three possible sources that may lead to the symmetry breaking: a misalignment of the applied field, anisotropy axis, or the presence of strong second-order anisotropy. As a comparison with the existing approximated method, we will be focusing on the first case.

As one can imagine from the shape of the modified astroid in Figure 4.3(b), reaching the part of the straight switching lines beyond the zero-current barriers in the j-h phase diagram requires the field to get into the bubble region from the main body of the modified astroid, and the bottleneck serves as a bridge between the two. From the discussion in the previous section and the Figure 4.6, the trajectory of the external field must go through the tunnel without touching the S_+ curves to prevent early switching. In the distorted astroid calculated using the approximated method, there is no such a tunnel and therefore it prohibits the possibility that the field can enter into the bubble region without touching the switching boundary, this causes the infinite vertical switching boundaries in the analytical j-h phase diagrams (see Figure 13 in Ref. [17]).

The symmetry breaking switching with a misaligned field pointing downwards for different tilt angles is illustrated in Figure 4.7. When is angle is small enough so that the field trajectory does not touch the S_+ curve, the P state evolves smoothly and is destabilized when the field crosses the bottom of the bubble, as shown in the left panels in Figure 4.7. This intersection point composes the linear portion in the j-h phase diagram. When the angle is big enough so that the field trajectory crosses the triangular before entering into the bubble region, three intersections with the three critical curves can be plotted along the trajectory, as shown in Figure 4.7(top right). At the intersection with S_+, the P state merges with the saddle point, which is created
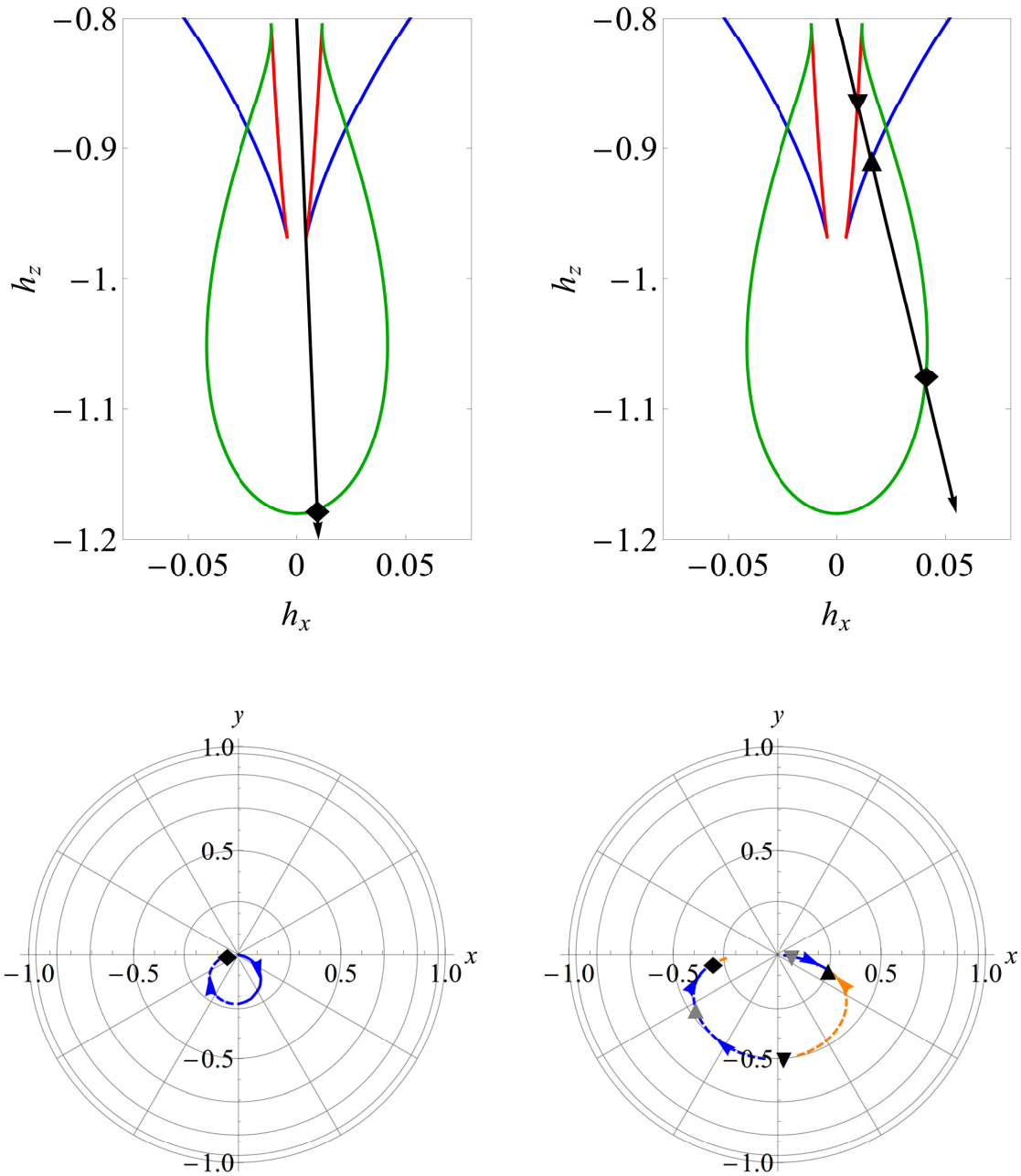
Figure 4.7: Switching in a slightly misaligned axial field. Top left: field trajectory through the bottleneck tunnel; Bottom left: evolution of the P state viewed at the top of the magnetization unit sphere; Top right: field trajectory through the triangular region; Bottom right: evolution of the P state accompanied with two other states viewed at the top of the magnetization unit sphere, the creation and annihilation of states take place at $S_\pm$. The blue lines are trajectories of sinks, the orange lines are trajectories of source and saddle. Two simultaneous critical events are marked with the same label, i.e., the inverse triangles in the right panels indicate that two equilibria are created when the field crosses the red line.

39

along with another stable state at the intersection with S_-, and the early switching occurs. Since the shape of S_+ does not vary much with the current, when the tilt angle is small, this reversal always happens approximately at $h = h_c(j = 0)$. In the j-h phase diagram, it give rises to the two vertical barriers near the zero-current fields. Besides, if the combination of current and field is able to perform a trajectory similar to the U-shape one shown in Figure 4.6, which means that the field first enters into the bubble region through the tunnel and then crosses the triangular region by going backwards, it may lead to a switching when the field crosses S_- or S_T. In terms of the j-h phase diagram, this backwards crossing gives rise to two additional parts close to the two vertial barriers. The exact j-h phase diagram is plotted in Figure 4.8 for two different angles, it shows some similarities with the numerical simulated diagrams in those references but also exhibits some features that are not able to capture by simulation.

The thickness of the bottleneck, which becomes critical in determining the switching, can be estimated as

$$\Delta h \approx 4\left(g\Big|_{\theta=0}\frac{j}{j_0}\right)^{3/2} \qquad (j/j_0 > 0), \tag{4.12a}$$

$$\Delta h \approx 4\left(g\Big|_{\theta=\pi}\frac{j}{j_0}\right)^{3/2} \qquad (j/j_0 < 0). \tag{4.12b}$$

For $j/j_0 = 0.1$ and $P = 50\%$ this approximation gives $\Delta h = 9.71 \cdot 10^{-3}$ in good agreement with the actual bottleneck width $\Delta h = 9.68 \cdot 10^{-3}$.

Besides the misalignment of the applied field, the misalignment of the anisotropy easy axis with the polarizer may also lead to the result. In that case the rotational symmetry of the astroid is broken and one must represent it in a three-dimensional fashion. Consiquently, the tunnel does not have a spherical shape cross section and may disconnect when the current is not sufficiently large. In addition, because of the narrowness of the tunnel, the thermal fluctuation may also lead to the switching when field crosses the bottleneck. However, our analytical approach is only able to

40
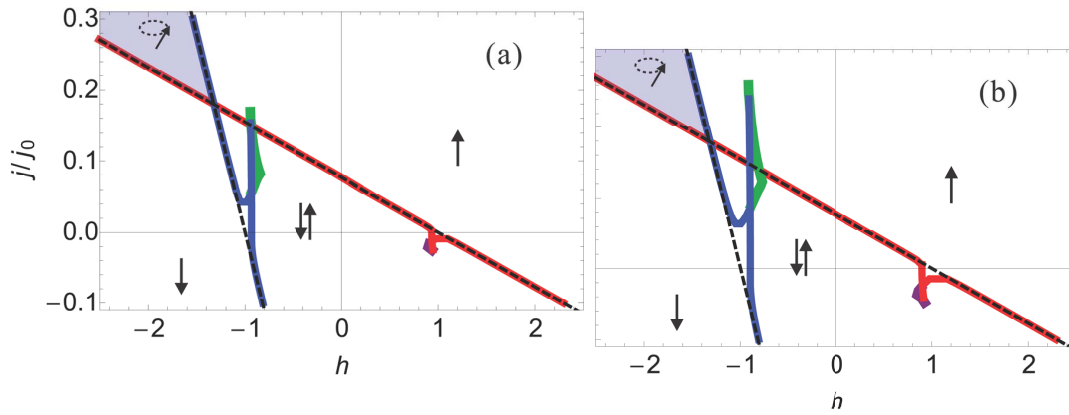
Figure 4.8: Switching phase diagrams for a misaligned field with the tilt angles (a) $\tan \beta = 0.01$, and (b) $\tan \beta = 0.02$. The dashed lines show the critical curves with the field strictly aligned with the easy axis, given by Eq. 4.11. The up and down arrows indicate P state and AP state, respectively. The gray region indicates the precession state. Note that the green line close to the blue line (the purple line close to the red line) indicates the switching happens when the j-h trajectory crosses it from left to right (from right to left), opposite to the normal switching direction.

deal with the system at $T = 0K$. In order to take the fluctuation into account, one needs to include a stochastic force into the model.

CHAPTER 5

APPLICATION IN BILAYER SHE DEVICES

The spin Hall effect (SHE), a relativistic spin-orbit coupling phenomenon that can be used to generate spin polarized currents in non-magnetic systems, was proposed by Dyakonov and Perel in 1971 [19]. But the term "spin Hall effect" was introduced almost 30 years later, by Hirsch in 1999 [27]. In the article he proposed a device in which the anomalous skew scattering of the moving magnetic moments causes spin imbalance, in a direction perpendicular to the current flow. The spin polarized current is injected into another part and detected via inverse spin Hall effect (iSHE). Zhang [100] derived the spin Hall effect in the presence of spin diffusion from a semiclassical Boltzmann equation and suggested that the edge spin accumulation could be detected by an attached ferromagnetic probe. Inspired by studies of the intrinsic anomalous Hall effect (AHE) in ferromagnets, Murakami et al. [60] and Sinova et al. [72] predicted that a spin transverse deflection of electrons in non-magnetic systems can originate directly from the relativistic band structure of the conduction without involving the Mott scattering. The theoretical debates and the experimental results are summarized in several review articles [70, 62, 88, 33].

The application of spin-polarized current due to SHE has been limited by its modest strength. The spin Hall angle[1] for Pt reported by Morota et al. in 2011 [59] was 0.021, although this value is about six times larger than the previous measurement, 0.0037 [89]. By measuring the spin-torque ferromagnetic resonance in a Pt/Py bilayer

---

[1]The spin Hall angle is defined as $\theta_{\mathrm{SH}} = j_{\mathrm{S}}/j_{\mathrm{e}}$, where j is the charge current density and $j_{\mathrm{S}}\hbar/2e$ is the spin current density arising from the SHE.

thin film, Liu et al. estimated the spih Hall angle for Pt to be 0.076 [46]. In 2012, Liu et al. reported a giant SHE in β-Ta with spin Hall angle to be $\theta_{\mathrm{SH}} = 0.12 \backsim 0.15$, that generates spin currents intense enough to induce efficient spin-torque switching of ferromagnets at room temperature [47].

Besides the bulk SHE, in studying the bilayer structures consisting of ferromagnetic layers and nonmagnetic heavy-metal layers, another mechanism [48, 49] was proposed which takes into account the Rashba spin-orbit coupling [16] by modeling the bilayer as two dimensional electron gas with strong inversion symmetry breaking in the direction perpendicular to the two-dimensional plane.

In this chapter we will be focusing on the switching phase diagram in the SHE based spintronic devices.

5.1 Spin torques generated by the SHE

Recently a number of researches have been focused on bilayer structures consisting of ferromagnetic layers and nonmagnetic heavy-metal layers such as Pt, Ta or W [3, 55, 67, 46, 54, 90, 45, 47, 63, 37]. It is theoretically predicted and experimentally observed that, when an in-plane current is being applied, the itinerant electrons inside the nonmagnetic layers become spin polarized due to the strong spin-orbit coupling and exert magnetic torques on the ferromagnetic layers. These additional torques contribute to the magnetization dynamics as described by the Landau-Lifshitz-Gilbert equation. Up to now two different pictures have been proposed to account for the effects. One treats the bilayer structure as a two-dimensional system with strong interfacial Rashba spin-orbital coupling [55, 54]. This model leads to a field-like torque of the form $\hat{\mathbf{m}} \times (\mathbf{j}_e \times \hat{\mathbf{z}})$ [48, 49, 53, 23, 25], where $\hat{\mathbf{m}} = \mathbf{M}/M_s$ is the magnetization unit vector, $\mathbf{j}_e$ is the in-plane current density, and the interface normal is pointing along the $\hat{\mathbf{z}}$ direction. The other [3, 46, 90, 45, 47, 63] is based on the interfacial diffusion of in-plane spin-polarized current which arises from the nonmagnetic layers
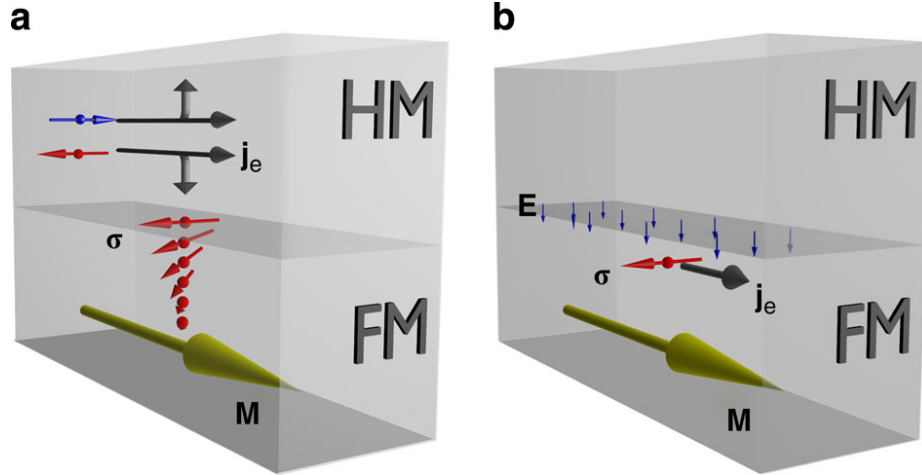
Figure 5.1: Sketches of two mechanisms for spin orbital torque and field. (a) SHE: electric current through the HM layer generates a spin current via SHE. The spin current exerts an effective torque and field on the adjacent FM layer via the spin transfer effect. (b) Rashba effect: an electric current through the interface between HM and FM layer experience a Rashba field via the spin-orbital interaction under the structural inversion asymmetry. Through the exchange coupling and spin relaxation, the Rashba effect exerts an effective field as well as a torque on the FM. Diagram from Ref. [20].

due to the bulk spin Hall effect (SHE)[27, 100, 72, 33] and leads to spin transfer torque (STT) dynamics[73, 68] in the magnetic layers. In the diffusion model the torque is directed along $\hat{\mathbf{m}} \times [\hat{\mathbf{m}} \times (\mathbf{j}_e \times \hat{\mathbf{z}})]$ [25] which has a damping-like form.[2]

For perpendicularly magnetized magnetic layers, several experiments have observed that the in-plane current could switch the magnetization of the magnetic layers [54, 45, 47]. The magnetic reversal is believed to be induced by the damping-like torque only for the following reasons: (1) the experimentally measured switching phase diagrams are accord with the macrospin model calculations within the error range, and (2) the field-like torque, if there is any, does not favor either states due to its symmetry and therefore should not contribute to the switching. Besides the diffusion model, some later calculations suggest that the Rashba-model also generates similar damping-like torques and should be responsible to the switching as well

---

[2]This torque is also referred as Slonczewski-like spin transfer torque in some literature.

[38, 65].

Despite the fact that the underlying mechanism is still not fully understood, a thorough study of the switching behavior based on the existing experimental results is of importance to analysis and prediction. However, unlike in the cases of spin valves or magnetic tunnel junctions (MTJs) with the polarizers designed to be parallel to the easy axis of the free layers, the lack of rotational symmetry in this configuration incapacitates the application of the small current, two-dimensional approximation.

In the following sections of this chapter, we apply the method of finding the critical surfaces to the bilayer systems with perpendicular uniaxial anisotropy and an in-plane current which generates a damping-like torque with its strength proportional to the current density. The field-like torque in the Rashba model, on the other hand, can be compensated by an external field in the direction opposite to the spin polarization and therefore only shifts the overall results accordingly.

5.2 CRITICAL SURFACES IN A SHE DEVICE

We first construct the three-dimensional critical surfaces of a bilayer SHE device. The dimensionless perpendicular uniaxial anisotropy energy has the same form as in the spin valve case and is given by Eq. (4.2). We set the in-plane current to be along the $+\hat{\mathbf{y}}$ direction, and assume the spin torque strength does not depend on the angles, i.e., $g(\theta, \phi)$ is a constant, which is usually considered to be the case, then the current induced spin-transfer-torque field can be written as

$$\mathbf{h}_{\mathrm{st}} \propto \hat{\mathbf{m}} \times (\mathbf{j} \times \hat{\mathbf{z}}) = \alpha_j \hat{\mathbf{m}} \times \hat{\mathbf{x}}, \tag{5.1}$$

where α_j is a strength parameter proportional to the current density. The rotational symmetry is no longer preserved due to this additional torque, and therefore the corresponding critical λ values should depend on both θ and ϕ. Substituting ε from
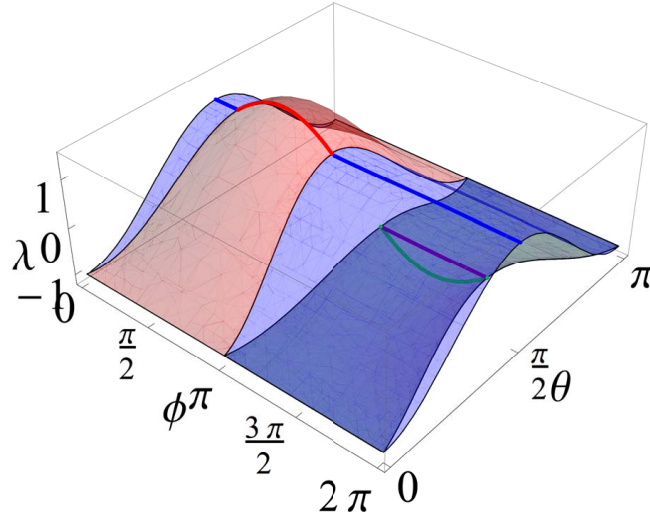
45

Figure 5.2: The λ_+ and the λ_T are shown by blue and purple surfaces, respectively. The dark green area below λ_+ is composed of λ_- and another piece of λ_T, one on top of the other. The damping parameter and the spin torque strength are set to be $\alpha = 0.1$ and $\alpha_j = 0.1$.

Eq. (4.2) and $\mathbf{h}_{st}$ from Eq. (5.1) into Eq. (3.17) and Eq. (3.18), we get

$$\lambda_T = \frac{\sin^2\theta}{2} - \cos^2\theta - \frac{\alpha_j}{\alpha}\sin\theta\cos\phi, \qquad (5.2)$$

$$\lambda_\pm = \frac{\sin^2\theta}{2} - \cos^2\theta \pm \sin\theta\sqrt{\frac{\sin^2\theta}{4} - \alpha_j^2\cos^2\phi}. \qquad (5.3)$$

The critical λ values are now functions of both θ and ϕ, and therefore should be plotted in three-dimensional space. Similar to the spin valve case, when the applied current is large enough, the λ_T surface may exceed the region enclosed by λ_- and λ_+ surfaces and the switching boundaries are determined according to criterion (3.19). Figure 5.2 shows the critical λ surfaces that are responsible for switchings. As one can see, part of the λ_+ is replaced by the λ_T above it and part of the λ_- also becomes critical together with the corresponding λ_T below it.

To plot the critical field surface, we first decompose the external field (3.14) into
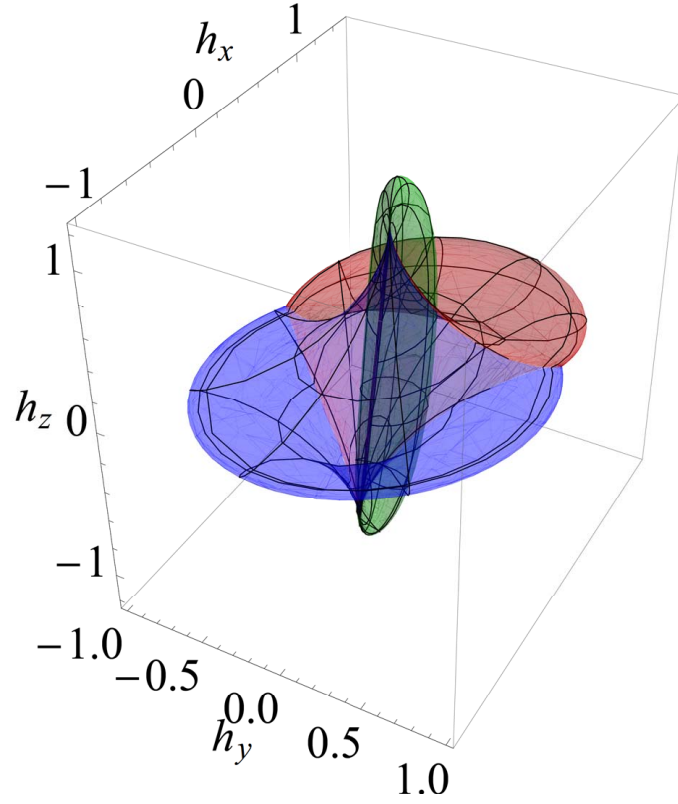
Figure 5.3: The critical surface in three-dimensional field space. The same color convention and parameters as in Figure 4.2 are adopted.

Cartesian coordinates as

$$h_x = (\lambda + \cos^2\theta)\sin\theta\cos\phi, \tag{5.4a}$$

$$h_y = (\lambda + \cos^2\theta)\sin\theta\sin\phi - \alpha_j\cos\theta, \tag{5.4b}$$

$$h_z = (\lambda - \sin^2\theta)\cos\theta + \alpha_j\sin\theta\sin\phi. \tag{5.4c}$$

The angle ϕ is no longer eliminable and we need to plot the entire surfaces in a three-dimensional field space. The corresponding critical surface is plotted in Figure 5.3.

5.3 Phase diagram in the Y-Z plane

The switching phase diagram in the y-z field plane is of importance to experiments because it requires the smallest field for magnetization switching to happen in this configuration. The fact that the spin-transfer torque shifts the existing equilibria clockwise or anticlockwise within the same plane makes it a two-dimensional problem, which draws attentions to theoretical calculations. However, earlier studies of a similar configuration show that when the spin torque strength is large enough, it generates a region in field space with all in-plane equilibria being destroyed, which means there must be some even number of out-of-plane equilibria existing according to Poincaré-Hopf theorem. Here we give a complete study of the phase diagrams.

When the external field is confined in the y-z plane, it is easy to see that the constraint $h_x = 0$ indicates either $\phi = \pm\pi/2$, or $\lambda = -\cos^2\theta$, or $\theta = \{0, \pi\}$, according to Eq. (5.4a). The last case, in which the equilibrium states are at two poles, is trivial and can be automatically included into the first case. We now focus on the first two non-trivial cases.

Case 1: if $\phi = \pm\pi/2$, the set of equilibrium states are also in the field plane, which is now y-z plane. We refer them as in-plane (IP) equilibria. It is obvious to see from Eqs. (5.2) and (5.3) that λ_{T} is always the midpoint of $\lambda_{\pm}$, same as in the conventional case. Therefore only λ_+ is needed to calculate the critical surface. By substituting $\lambda = \lambda_+$ and $\sin\phi = \pm1$ into Eqs. (5.4b) and (5.4c), we get a parametric form of the critical field in the y-z field plane

$$\begin{cases} h_y = \pm\sin^3\theta - \alpha_j\cos\theta \\ h_z = -\cos^3\theta \pm \alpha_j\sin\theta \end{cases} \tag{5.5}$$

The critical field above describes a modified Stoner-Wohlfarth (SW) astroid which is squeezed along one of its diagonal lines. We will refer it as IP phase diagram since it describes the merging of IP equilibria only.

48

Case 2: if $\lambda = -\cos^2\theta$, then we have $h_y = -\alpha_j\cos\theta$ and $h_z = -\cos\theta + \alpha_j\sin\theta\sin\phi$. It corresponds to two out-of-plane (OOP) equilibria with their angles satisfying $\cos\theta = -h_y/\alpha_j$ and $\sin\phi = (h_z - h_y/\alpha_j)/\sqrt{\alpha_j^2 - h_y^2}$. Taking into account the range of trigonometric functions, the critical field that generates the two OOP equilibria, one on each half of the unit sphere, is given by

$$\begin{cases} h_y = -\alpha_j\cos\theta, \\ h_z = -\cos\theta \pm \alpha_j\sin\theta. \end{cases} \tag{5.6}$$

If we substitute $\lambda = \lambda_-$ into Eqs. (5.4b) and (5.4c) with $\sin\phi = \pm 1$, we will get exactly the same critical field as Eq. (5.6). This is not coincidence but the physical meaning of λ_-: the two OOP equilibria first emerge in pair with $\sin\phi = \pm 1$ and then move out of y-z plane as long as the field is being increased. Since S_+ is responsible for the IP equilibria, the emergence of OOP therefore should be captured by S_- in y-z plane.

Next we analyze their stabilities. When $\lambda_\pm$ are real, $\lambda \leqslant \lambda_-$ is always satisfied according to Eq. (5.3). Combining with the situation when $\lambda_\pm$ are complex, the stability criteria simply require

$$\lambda - \lambda_{\mathrm{T}} = \left(\frac{\alpha_j}{\alpha}\cos\phi - \frac{1}{2}\sin\theta\right)\sin\theta > 0. \tag{5.7}$$

The equilibrium located in the $-x$ half of the unit sphere is always unstable because $\lambda - \lambda_{\mathrm{T}}$ remains negative when $\cos\phi < 0$. The other one in the $+x$ half can be stable if the inequality (5.7) is satisfied. This condition leads to another critical field given by

$$\begin{cases} h_y = -\alpha_j\cos\theta, \\ h_z = -\cos\theta \pm \sin\theta\sqrt{\alpha_j^2 - \alpha^2\sin^2\theta/4}. \end{cases} \tag{5.8}$$

We refer Eq. (5.8) as OOP phase diagram since it gives the destabilization boundary of the OOP equilibrium in the $+x$ half of the unit sphere.

The IP and OOP phase diagrams give the complete switching phase diagrams in the y-z field plane. For $\alpha_j < 1/2$, the IP phase diagram is topologically equivalent

49

to the conventional Stoner-Wohlfarth astroid and the equilibrium merging process is similar: there are four equilibria when the field is inside the astroid and a stable equilibrium merges with a saddle point when it crosses the boundary from inside. For $\alpha_j > 1/2$, the IP phase diagram becomes self-crossed and there will be no IP equilibria when the field is within the self-crossed area since it is equivalent to cross the boundary twice along the direction of merging. Nevertheless, the diagram (5.6) always covers the area which guarantees the existence of at least two equilibrium states and therefore Poincaré-Hopf theorem is not violated.

In addition to the conventional IP switching, if the field moves to the area outside the IP phase diagram but still inside the OOP phase diagram, the magnetization could switch to the stable OOP equilibrium. In addition, since the OOP phase diagram is a function of damping parameter α, in the high damping, high current regime, the system is possible to get into a state with two unstable OOP equilibria and no IP equilibria. In this case the magnetization will precess along a limit cycle. Figure 5.4 shows the phase diagrams for varying spin torque strengths and damping factors. The diagrams with negative currents can be get by reflection with respect to the z axis.

5.4 THRESHOLD SWITCHING CURRENTS

According to the discussion in Sec. 5.3, the magnetization can be switched to either an IP equilibrium or an OOP equilibrium, depending on the combination of external field and spin-transfer torque. According to the numerical simulation, if the switching condition is met and both IP and OOP equilibria are present, the magnetization will be switched to the OOP equilibrium instead of the IP equilibrium. Consequently, the threshold switching currents should reflect two scenarios: IP switching and OOP switching. The threshold currents as functions of field are plotted in Figure 5.5 with the field applied along three different directions. The IP switching and OOP switching

50

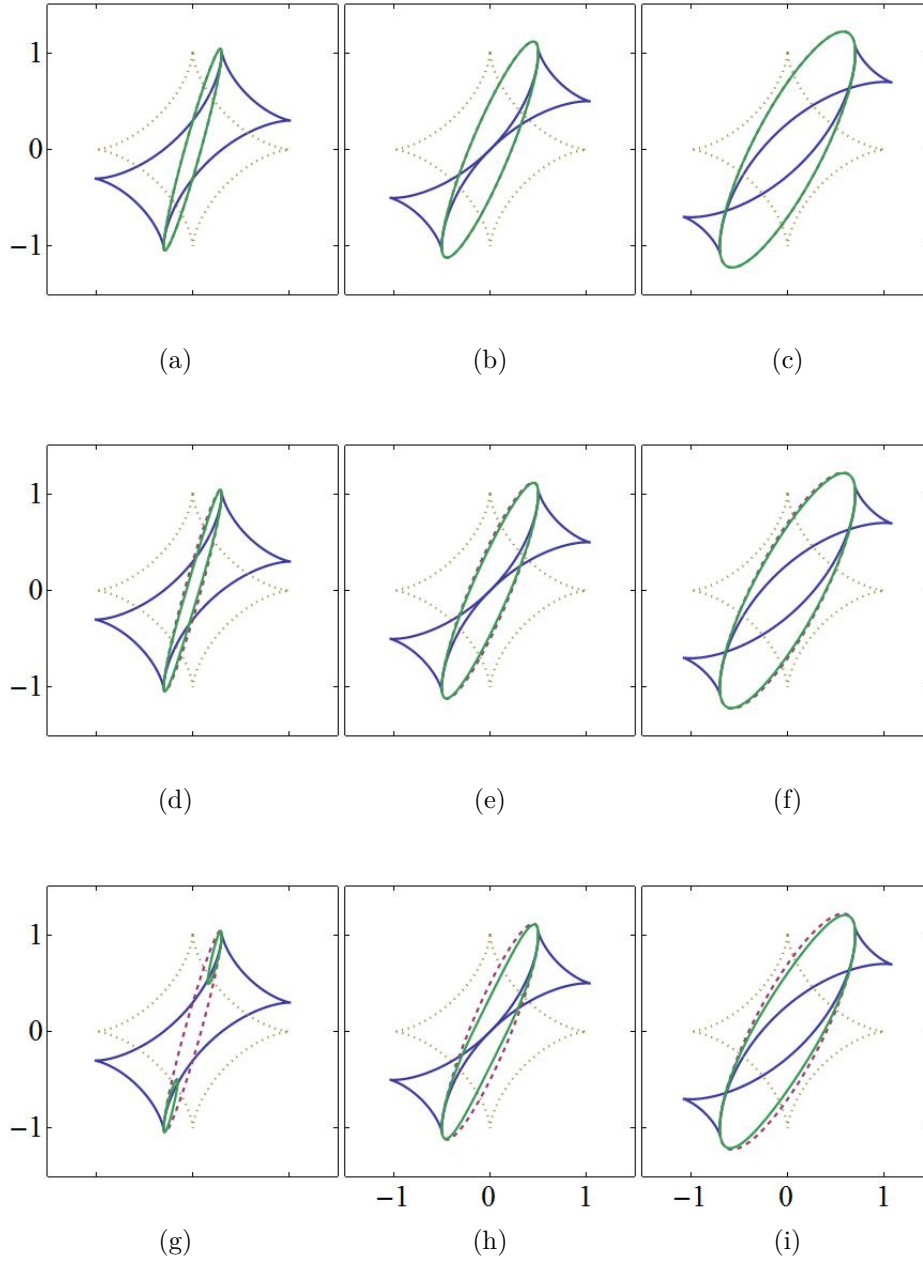Figure 5.4: The blue and green solid curves are IP phase diagrams and OOP phase diagrams, respectively. The purple and brown dashed curves are OOP critical fields (5.6) and conventional SW astroids, respectively. The varying spin torque strengths and damping factors are: α_j is set to be 0.3, 0.5 and 0.7 from left column to right column, α is set to be 0.1, 0.4 and 0.7 from top row to bottom row.

are separated by the line intersections as shown in the figures. Comparing with the IP switching, the OOP switching favors a smaller external field but relatively large current. High damping also prohibits the OOP switching.
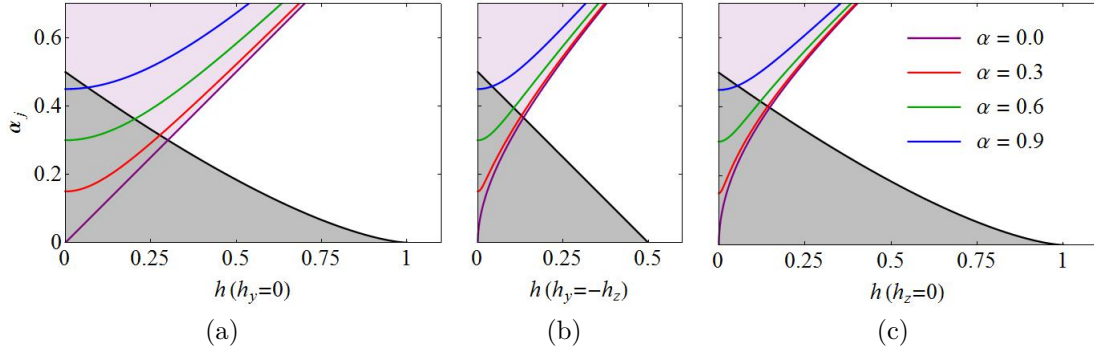
Figure 5.5: The threshold switching current (spin torque strength) with field applied along the following directions: left panel $-\hat{\mathbf{z}}$, middle panel $\hat{\mathbf{y}} - \hat{\mathbf{z}}$, and right panel $\hat{\mathbf{y}}$. The switching regions are separated into two parts which correspond to OOP switching (light purple) and IP (white) switching, respectively.

However, since the OOP and IP equilibria coexist in the OOP switching, is it possible that $\hat{\mathbf{m}}$ switches to the IP equilibrium instead of the other? The answer is no. From Figure 5.6 we can see that, when OOP switching condition is met, one can find such a curve that passes the IP saddle point and separates the entire plane into two parts, each of which has a sink within it. When the initial condition starts from the upper half of the unit sphere, there is no path that connects it to the IP sink. Therefore the only possible switching in this case is toward the OOP sink.

Figure 5.6: The magnetization flow in the θ-ϕ plane in the case of OOP switching. The OOP sink, OOP source, IP saddle and IP sink are ma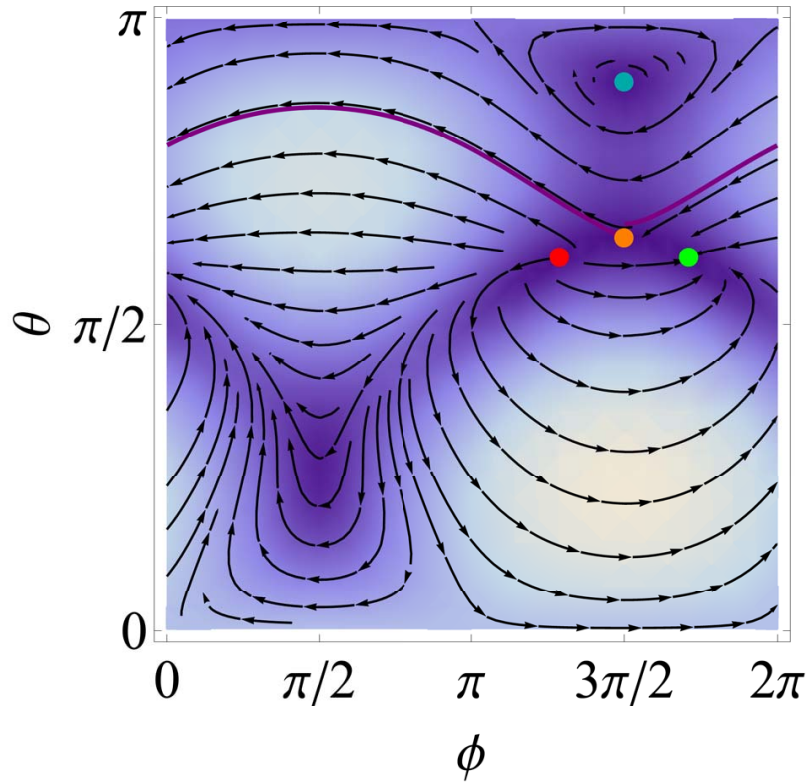rked by green, red, orange and blue dots, respectively. The purple curve separates the plane into two parts. The background color denotes the strength of the flow. The parameters are set to $h_y = 0.15$, $h_z = 0$, and $\alpha_j = 0.45$.

CHAPTER 6

MAGNETIZATION SWITCHING PROCESS

Magnetization reversal is one of the most important processes in magnetism that is linked to the magnetic data storage process such as currently used in hard disk drives. Therefore switching speed and reliability are two crucial factors to the design of such systems.

In the macrospin model, "damping" and "precessional" magnetization switchings are two mostly considered switching scenarios so far. In the damping switching mode, both the external field and the spin polarization point opposite to the initial state and the magnetization moves towards the new equilibrium gradually along a spiral trajectory which is considered to be reliable but quite slow [13, 68, 9, 6]. Much faster reversals, which are often classified as precessional switchings, have been designed with either the field applied at a certain angle (usually orthogonal) or the spin polarization perpendicular to the free layer easy axis [5, 36, 44]. In both cases the effective torque pushes the magnetization out-of-plane, creating a strong demagnetizing field in the direction perpendicular to the easy axis. However those reversal processes require fields or current pulses perfectly fit the precession frequency which increases the error rate and is experimentally hard to control.

In this chapter we first review some discoveries for damping and precessional switchings, then we analyze a novel switching scenario which has been brought into attention recently. For comparison purpose, the analytical studies are performed

using the dimensionless LLG equation (2.9) in spherical coordinates

$$\begin{cases} \dot{\theta} = h_{\text{eff}}^{\phi} + \alpha h_{\text{eff}}^{\theta}, \\ \sin\theta\dot{\phi} = -h_{\text{eff}}^{\theta} + \alpha h_{\text{eff}}^{\phi}. \end{cases} \tag{6.1}$$

Thermal stochastic excitations are not considered in the calculations.

6.1 DAMPING SWITCHING

An analytical solution for damping switchings can be found when the external field and spin polarization are both parallel with the easy axis. In this case the effective field is written as

$$\mathbf{h}_{\text{eff}} = (m_{\text{z}} + h)\hat{\mathbf{z}} + h_{\text{st}}(\theta)\hat{\phi}, \tag{6.2}$$

where $h_{\text{st}}(\theta)$ is given by Eq. (4.4). Since the effective field is now only a function of θ, the second equation in Eq. (6.1) is trivial and the first one becomes

$$\dot{\theta} = -\left[\frac{jg(\theta)}{j_0} + \alpha(\cos\theta + h)\right]\sin\theta \tag{6.3}$$

The successful switching from $\hat{\mathbf{z}}$ to $-\hat{\mathbf{z}}$ (or from $-\hat{\mathbf{z}}$ to $\hat{\mathbf{z}}$) requires the right hand side of Eq. (6.3) to be always negative (positive), which determines the threshold current as a function of the external field. Figure 6.1 shows the threshold switching currents with $g(\theta)$ given by the Slonczewski's function (Eq. (2.12)) and $g(\theta)$ equals a constant. In the first case, the asymmetry of $g(\theta)$ causes the two threshold current line intersects and the magnetization may enter into a limit cycle state in which the energy gained from the spin-transfer torque during each cycle of precession is balanced by the energy lost to damping, whereas in the second case, the two threshold current line are parallel and the magnetization vector is reversed once the switching condition satisfies.

In addition to the above condition, the switching also requires the initial value of $\hat{\mathbf{m}}$ to deviate from $\hat{\mathbf{z}}$. In reality, due to thermal effects, $\hat{\mathbf{m}}$ always slieghtly fluctuates
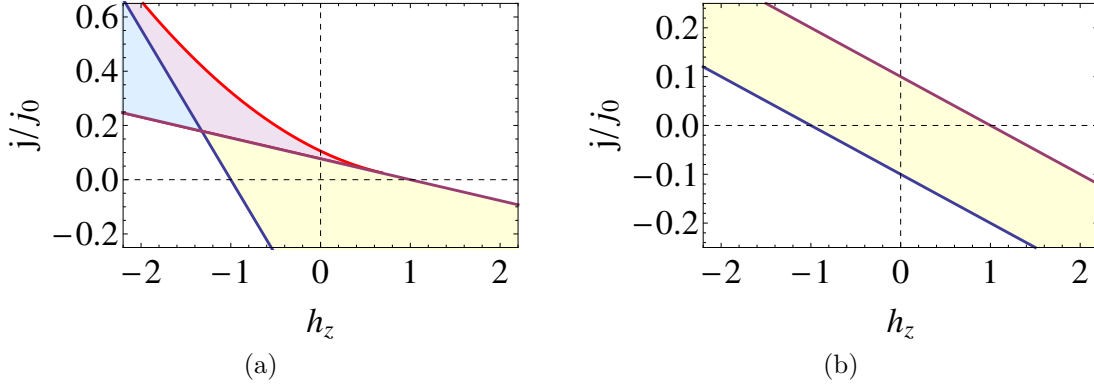
Figure 6.1: The critical switching lines in the damping switching mode with (a) $g(\theta)$ given by Eq. (2.12), and (b) $g(\theta) = 1$. In both figures, the blue and purple lines are the switching boundaries of $\hat{\mathbf{z}}$ and $-\hat{\mathbf{z}}$ states, respectively. In figure (a), the blue region indicates the limit cycle mode, the light purple region indicates the coexistence of the $\hat{\mathbf{z}}$ state and the limit cycle mode.

around the equilibrium state $\hat{\mathbf{z}}$, which will make the switching to happen. From Figure 6.2, we can see that the initial stage of switching process is very sensitive to the initial value, smaller initial angle requires much longer time precessing away from $\hat{\mathbf{z}}$. Besides, the switching time is also affected by the external field and the spin-transfer torques, which are illustrated in Figure 6.3.
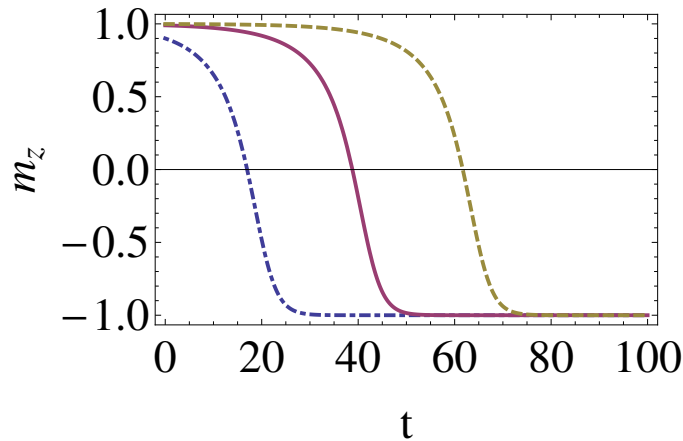

Figure 6.2: Time evolution of m_z for $z_0 = 0.9$ (blue dot-dashed line), $z_0 = 0.99$ (purple solid line), and $z_0 = 0.999$ (brown dashed line). The parameters are $\alpha = 0.1$, $j = 0$, and $h = 1.5$.

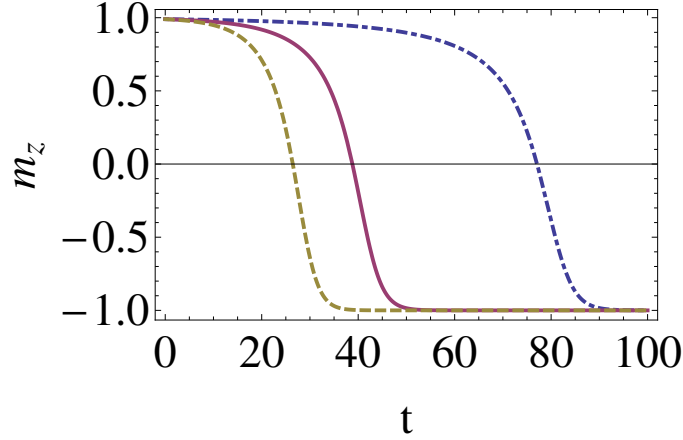The switching time can be derived by separation of variables, which leads to the

Figure 6.3: Time evolution of m_z for different external fields and spin-transfer torques. Same switching behaver is achieved by changing either the field, or the spin-transfer torque, or both, provided that h' are the same in each configuration. In this figure, they are $h' = 1.2$ (blue dot-dashed line), $h' = 1.5$ (purple solid line), and $h' = 1.8$ (brown dashed line). The initial value is set to be $z_0 = 0.99$. The rest parameters are the same with figure 6.2.

following integral

$$t = -\frac{1}{\alpha} \int_{\theta_0}^{\theta_t} \frac{1}{(h' + \cos\theta)\sin\theta} \mathrm{d}\theta, \tag{6.4}$$

where $h' = h + jg(\theta)/(\alpha j_0)$. For the $\hat{\mathbf{z}}$ to $-\hat{\mathbf{z}}$ switching, $h' < -1$ must be guaranteed. We further assume $g(\theta) = 1$ for simplicity, then the solution is calculated as

$$\alpha t = -\frac{1}{2(h'+1)} \ln\left(\frac{1-\cos\theta_t}{1-\cos\theta_0}\right) + \frac{1}{2(h'-1)} \ln\left(\frac{1+\cos\theta_t}{1+\cos\theta_0}\right) - \frac{1}{h'^2-1} \ln\left(\frac{h'+\cos\theta_t}{h'+\cos\theta_0}\right). \tag{6.5}$$

If the duration of the magnetic field pulse is such that a negative value of m_z is reached, then the magnetization will be in the basin of attraction of the equilibrium state $\hat{\mathbf{m}} = -\hat{\mathbf{z}}$, and the switching will be achieved. Therefore the minimum switching time τ can be found with $\theta_t = \pi/2$. This will lead to

$$\alpha\tau = \frac{1}{2(h'+1)} \ln(1-z_0) - \frac{1}{2(h'-1)} \ln(1+z_0) + \frac{1}{h'^2-1} \ln\left(1 + \frac{1}{h'}z_0\right), \tag{6.6}$$

where the z_0 has been substituted for θ_0. Note that when $h' \approx -1$, the first and the last term of the right hand side of Eq. (6.6) dominate, when $h' \ll -1$, only the first

57

one dominates. Therefore we can reach an approximated expression by keeping the first term and the leading order of the expansion of the last term, which is[1]

$$\alpha\tau = \frac{1}{2(h'+1)} \ln\left(h'\frac{1-z_0}{h'+z_0}\right) \qquad (6.7)$$

The exact and approximated switching time as functions of h' and m_z are plotted in Figure 6.4 and 6.5.
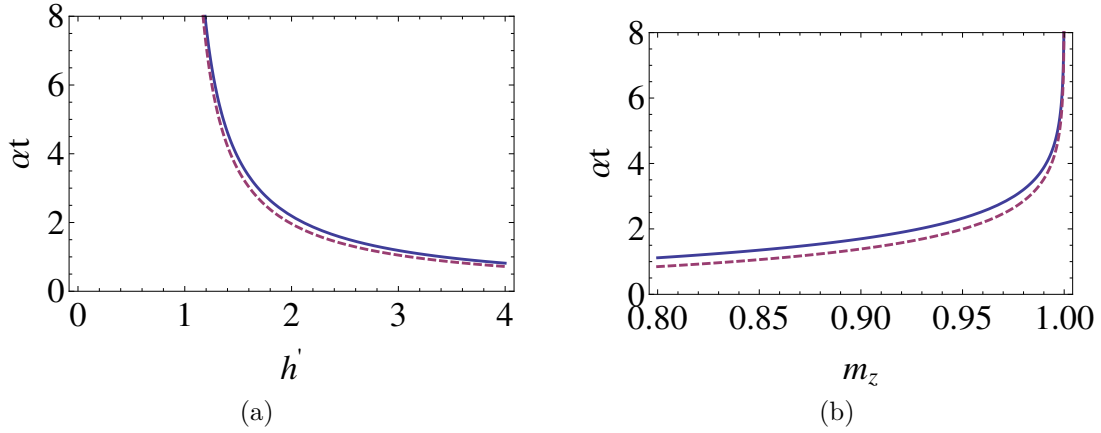
Figure 6.4: Dependence of switching time on (a) h' with $m_z = 0.99$, and on (b) m_z with $h' = -1.5$. The solid blue line and the dashed purple line are the exact and approximated solutions, respectively.
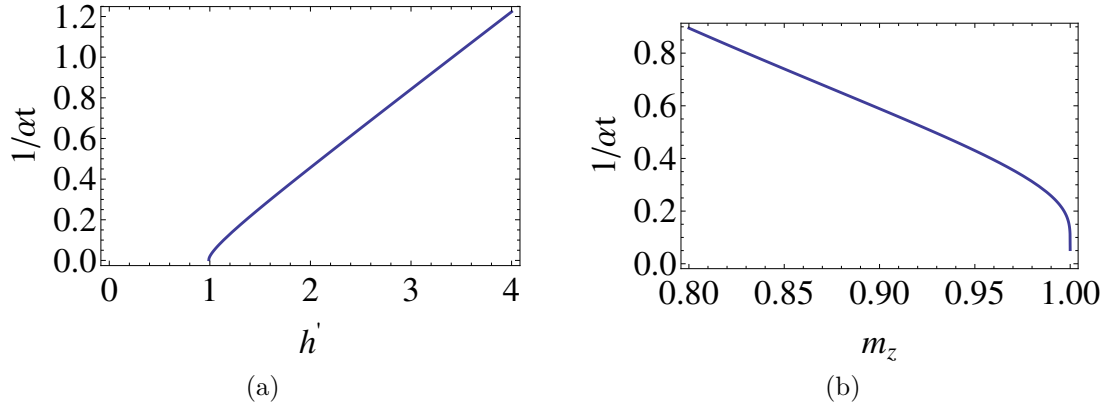

Figure 6.5: The reciprocal of switching time on (a) h' with $m_z = 0.99$, and on (b) m_z with $h' = -1.5$. Only the exact solution is shown in the picture.

---

[1]The minimum pulse time reported in Ref. [13] only keeps the first term of Eq. (6.6) which is valid in the large field regime only.

From the expression (6.7) it is apparent to see that the initial value of $\hat{\mathbf{m}}$ is crucial: smaller deviation angle means much longer switching time and therefore much longer field pulse is required. Although thermal fluctuation will cause the initial states deviate from absolute zero in reality, the randomicity of the fluctuation does not guarantee the switching to be always successful if the pulse length is not long enough. One possible solution is to break the rotational symmetry with precessional contribution by adding a small bias field perpendicular to the easy axis. When such a bias field is applied in addition to the switching field, the initial state $\hat{\mathbf{z}}$ is no longer an equilibrium and, since $\hat{\mathbf{m}}$ is away from the new equilibrium by roughly the same degree, the same switching time is guaranteed. By sweeping a tilted field from up to down at different speed, the switching also behaves differently. It turns out that faster sweeping rate does not always lead to shorter switching time. The numerical and analytical results are reported in Ref. [9] and [6]. However, compared with the precessional switching which will be discussed in the next section, damping switching is overall a reliable yet slow switching process.
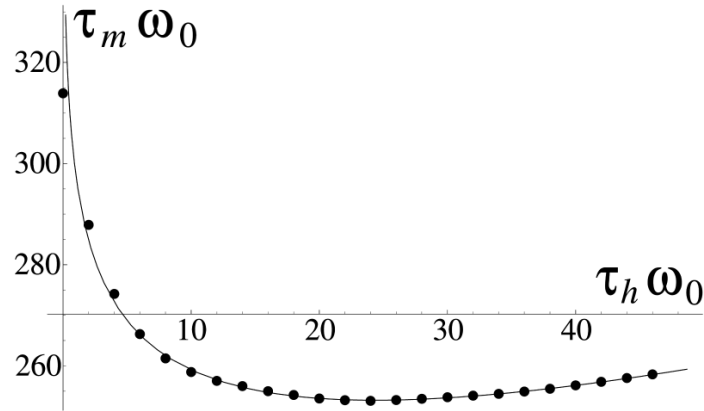

Figure 6.6: Dependence of switching time on field sweep time with a bias field. The dots are numerical values and the curve is the analytical solution. Parameter values are $\alpha = 0.01$, $h_\parallel = -3.5$, and $h_\perp = 0.001$. Diagram from [9].

6.2 Precessional switching

Precessional switching is another strategy to realize magnetization reversal which has been recently the focus of considerable research. In terms of the LLG equation, the precessional switching takes advantage of the first term on the right hand side of Eq. (2.9), and therefore is usually much faster than the conventional damping switching. In precessional switching, either the external field or the spin-transfer field can serve as the torque that pushes the magnetization out-of-plane.

Field-induced precessional switching

We first consider the case with the field applied along the y axis but no spin transfer torque applied. The effect field is then

$$h_{\text{eff}} = m_z \hat{\mathbf{z}} + h \hat{\mathbf{y}}. \tag{6.8}$$

Since the switching is mainly driven by the precessional torque term of the LLG equation, when α is small, we can simply ignore the damping term and the equation of motion is energy conservative

$$\frac{\mathrm{d}\hat{\mathbf{m}}}{\mathrm{d}t} = -\hat{\mathbf{m}} \times \mathbf{h}_{\text{eff}}, \tag{6.9}$$

The approximate trajectory becomes an equipotential line that connects $\hat{\mathbf{z}}$ and $-\hat{\mathbf{z}}$ on the unit sphere which therefore gives an integral of motion of such systems

$$\varepsilon = -\frac{1}{2}\cos^2\theta - h\sin\theta\sin\phi = -\frac{1}{2}. \tag{6.10}$$

Eq. (6.10) can be further reduced to

$$\sin\theta = 2h\sin\phi. \tag{6.11}$$

By substituting Eq. (6.8) and (6.11) into Eq. (6.9), we arrive at a nonlinear differential equation

$$2\ddot{\theta} + \frac{1}{4}\sin 2\theta = 0, \tag{6.12}$$

60

with the initial conditions satisfying $\theta(0) = 0$ and $\dot{\theta}(0) = h$. The equation above has the same form with the one that describes the simple pendulum. To find the solution, we turn to a different approach by using the first order differential equation derived from the θ component of Eq. (6.9)

$$\dot{\theta} = h \cos \phi = \pm h \left(1 - \frac{1}{4h^2} \sin^2 \theta \right)^{1/2}. \tag{6.13}$$

The equation above implies the switching field must be larger than a threshold value, $h > h_c = 0.5$. Note that the threshold field is inside the Stoner-Wohlfarth Astroid, this is because the initial state in this case is $\hat{\mathbf{z}}$ instead of the energy minimum. The solution is a periodic function (see Figure 6.7). In the presence of damping, $\hat{\mathbf{m}}$ will be attracted by one of the energy minima if $0.5 < h < 1$, depending on the initial values, or ended at $\hat{\mathbf{m}} = \hat{\mathbf{y}}$ if $h > 1$, where $\hat{\mathbf{y}}$ is the only energy minimum in that case.

Because of the periodicity, the switching time τ should be defined as from $\theta_0 = 0$ to $\theta_\tau = \pi$, therefore

$$\tau = \frac{T}{2} = \frac{2}{h} \int_0^{\pi/2} \left(1 - \frac{1}{4h^2} \sin^2 \theta \right)^{-1/2} \mathrm{d}\theta = \frac{2}{h} K \left(\frac{1}{4h^2} \right), \tag{6.14}$$

where $K(m)$ is the complete elliptic integral of the first kind.

It is important to point out that in the case of the precessional switching, the timing of switching off the field is crucial because of the periodicity of the trajectory, and the time window should satisfy $\tau/2 < t < 3\tau/2$.

Spin-transfer-induced precessional switching

Besides the external field, spin-transfer torque alone can also be used to induce the magnetic switching. The idea was first introduce A. D. Kent in 2004, in which a spin-current pulse produces a rapid reversal of the magnetization of a thin film nano-magnet. In their simulation they consider a current pulse consisted of a positive part and a negative part with equal time duration. The positive going part produces a

61
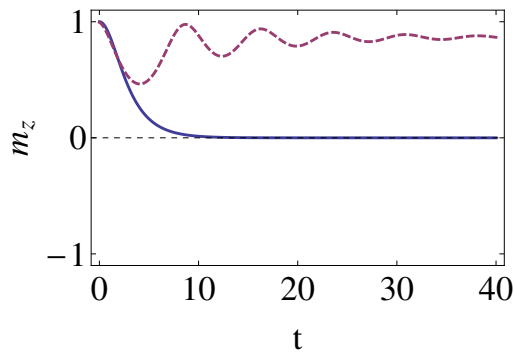
(a)
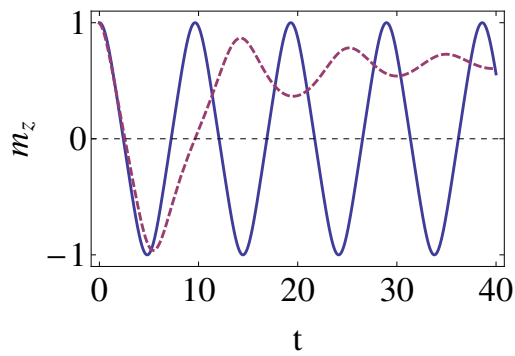
(b)
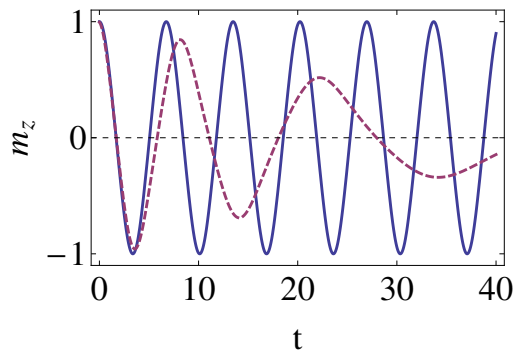
(c)

Figure 6.7: Precessional switching for different h in the cases of non-damping (solid lines) and of damping $\alpha = 0.01$ (dashed lines). The field h is set to be (a) 0.5, (b) 0.75, and (c) 1.
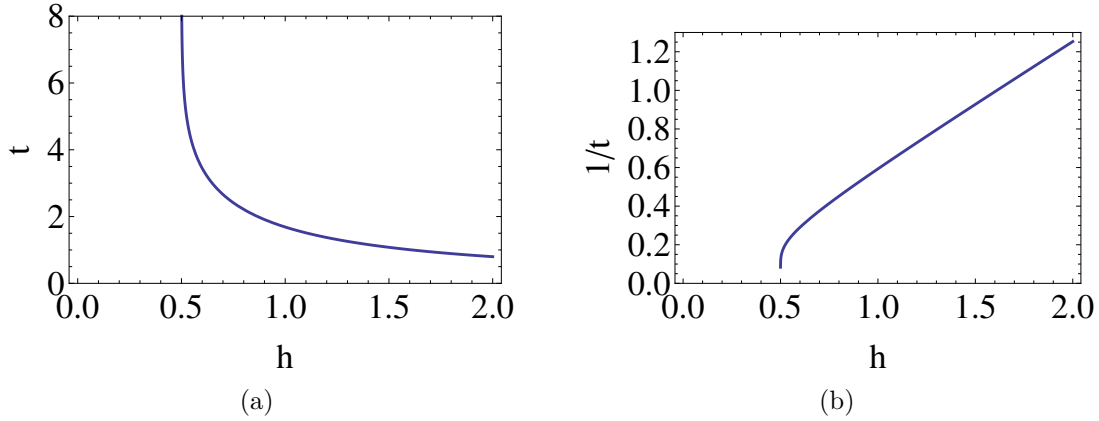
Figure 6.8: Dependence of switching time on h in the precessional mode.

torque that forces the magnetization of the free layer out of the film plane. This generates a demagnetization field mainly perpendicular to the film plane about which the magnetization precesses. The negative going part of the pulse pulls the magnetization back into the film plane stopping the precession in the desired state. In their simulation of a Co free layer with an in-plane uniaxial anisotropy $K = 7 \times 10^5 \mathrm{erg/cm^3}$ that is 3 nm thick, with lateral dimensions of 30 nm by 60 nm and the pulse current is $I_p = 5$ mA and P is 0.4. the reversal time T is 50 ps.

The theoretical limit in the magnetization reversal of SW nanomagnet is studied by X. R. Wang, et al. in one of their publications in 2007. They found the theoretical limit of critical currents which is far below the lowest critical current known today, showing a large room for future improvement. However, achieving the limit requires a precise manipulation to the polarized current, not only the magnitude, but also the polarization direction which makes it impractical.

6.3   SHE induced OOP switching

According to the discussion in Sec. 5.3, the magnetization can be switched to either an IP equilibrium or an OOP equilibrium. This provides a possible solution for fast and reliable magnetic reversals.

We consider the switch scenario that the magnetization, which is initially in the up state, is switched to the OOP equilibrium by a field and current pulse first. After the OOP state is obtained, if it is in the lower half of the unit sphere, it will relax to the down state by simply turning off the field and current. Note that $m_z = \cos\theta = -h_y/\alpha_j$, therefore from the viewpoint of reliability, the goal is to have larger h_y and smaller α_j, which suggests to choose the field along y direction. The dependence of angle θ on field and current is plotted in Figure 6.9.

The macrospin simulation is plotted in Figure 6.10. When the OOP switching condition is satisfied, $\hat{\mathbf{m}}$ will be directly switching to the OOP state without oscillation. Since the precessional term dominates the process, the damping α has negligible effect to this stage. It can be seen that the OOP switching takes roughly about the same time as the field induced precessional switching.
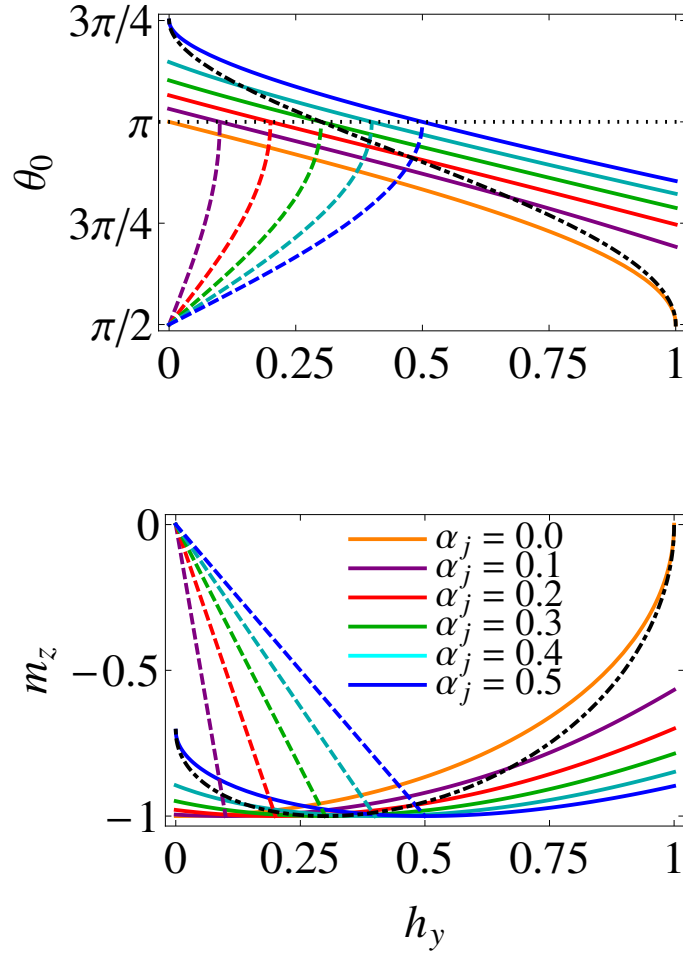
Figure 6.9: Upper panel: The polar angle θ of the intermediate states as a function of fields for varying currents. Lower panel: The $\hat{\mathbf{z}}$ components of the intermediate states. The IP equilibria and OOP equilibria are represented by solid lines and dashed lines in both panels, respectively. The solid lines above $\theta = \pi$ in the upper panel indicate the equilibria are in the $-y$ half of the unit sphere. The IP phase diagram is plotted with dot-dashed lines in both panels.

65
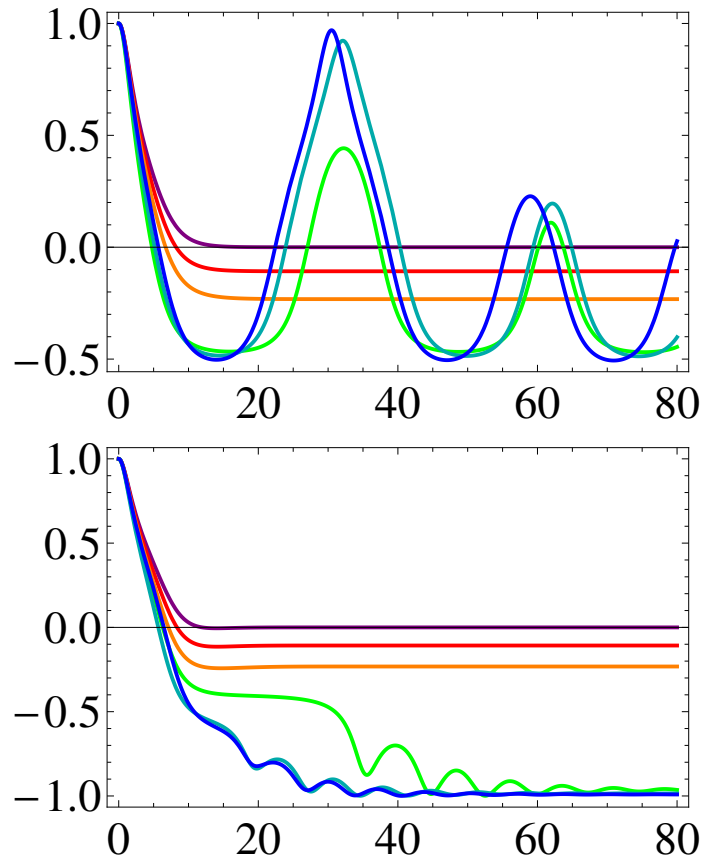
Figure 6.10: Simulation on the SHE induce switching with field along y axis. (a) low damping $\alpha = 0.001$, (b) high damping $\alpha = 0.1$. The parameters are: purple $h = 0$, $j/j_0 = 0.5$, red $h = 0.05$, $j/j_0 = 0.46$, orange $h = 0.1$, $j/j_0 = 0.42$, green $h = 0.15$, $j/j_0 = 0.38$, cyan $h = 0.3$, $j/j_0 = 0.34$, and blue $h = 0.25$, $j/j_0 = 0.30$. The first three configurations induce OOP switchings, the last three configurations induce IP switchings.

CHAPTER 7

CONCLUSIONS AND FUTURE WORK

In the present work we have theoretically investigated the stability properties of the magnetization of a single domain nanomagnetic layer in the presence of an external magnetic field, magnetic anisotropies and spin transfer torque. By disregarding the concepts of energy extreme and taking into account the different types of equilibria in terms of the asymptotic behaviors, we have derived the critical surfaces in an exact fashion that represent the different switching modes in general. In explaining the destabilization processes, it turns out that the λ-θ plane, by which each equilibria is tractable by its polar angles as well as its stability, could be more intuitive than the field plane.

The application to the spin valve nanopillar with perpendicular anisotropy not only recovers many features of the modified astroid that have been observed in experiment, but also predicts a novel region in which one more equilibrium is stabilized by the spin-transfer torque. This special region causes the destabilization depends on the field trajectory: by travelling through different paths, the destabilization will occurs at different points on the field plane. Finally, the "dented states" in the switching phase diagram that is observed in many experiments, which is believed to be caused by the breaking of rotational symmetry, is explained in the case with misaligned external fields.

The study on the switching phase diagram leads to two interesting topics: the misalignment of the polarizer with the free layer easy axis, and the destabilization caused by thermal fluctuations. The former issue could be directly solved using the

67

same approach, which should lead to a slight asymmetry in the modified astroid. The latter issue needs more studies on how to define the switching criterion in the presence of an stochastic force that represents the random walk of the magnetization.

In the case of SHE induced magnetic reversal, in which the rotational symmetry is broken, the phase diagram must be presented in an three-dimensional field space. We constructed the three-dimensional phase diagram using our approach and then focus on a special plane, where the astroid is distorted the most. We found that besides the existing in-plane equilibria, the spin-transfer torque also creates two out-of-plane equilibria, one on each side of the unit sphere. Therefore the phase diagram is composed of two separate diagrams. The different switching currents, which corresponds to IP switching and OOP switching, are analyzed.

In the last part we briefly reviewed the two distinct strategies of magnetic reversal and discussed their advantages and weakness. By noticing the special properties of the stable OOP equilibrium in the SHE induced switching, we proposed a new switching scenario which take advantages of the OOP equilibrium as the intermediate transit point. This new switching mechanism turns out to be as fast as the precessional switching without redundant precession.

An in-depth study on the OOP switching should be carried out, including the analytical study of the switching time, the optimal switching parameters, simulation on the switching stability in the presence of thermal fluctuations, and the possible experimental design, etc. This new switching strategy could be used to design the reliable ultra-fast switching based magnetic devices such as the MRAM.

Bibliography

[1]   Amikam Aharoni, *Introduction to the theory of ferromagnetism*, vol. 109, Oxford University Press, 2000.

[2]   Johan Akerman, *Toward a universal memory*, Science **308** (2005), no. 5721, 508–510.

[3]   K. Ando, S. Takahashi, K. Harii, K. Sasage, J. Ieda, S. Maekawa, and E. Saitoh, *Electric manipulation of spin relaxation using the spin hall effect*, Phys. Rev. Lett. **101** (2008), 036601.

[4]   M. N. Baibich, J. M. Broto, A. Fert, F. Nguyen Van Dau, F. Petroff, P. Etienne, G. Creuzet, A. Friederich, and J. Chazelas, *Giant magnetoresistance of (001)fe/(001)cr magnetic superlattices*, Phys. Rev. Lett. **61** (1988), 2472–2475.

[5]   M. Bauer, J. Fassbender, B. Hillebrands, and R. L. Stamps, *Switching behavior of a stoner particle beyond the relaxation time limit*, Phys. Rev. B **61** (2000), 3410–3416.

[6]   Ya B Bazaliy, *Analytic treatment of the precessional (ballistic) contribution to the conventional magnetic switching*, J. Appl. Phys. **110** (2011), no. 6, 063920.

[7]   Ya. B. Bazaliy, B. A. Jones, and Shou-Cheng Zhang, *Current-induced magnetization switching in small domains of different anisotropies*, Phys. Rev. B **69** (2004), 094421.

[8]   Ya B Bazaliy, BA Jones, and Shou-Cheng Zhang, *Towards metallic magnetic memory: How to interpret experimental results on magnetic switching induced by spin-polarized currents*, J. Appl. Phys. **89** (2001), no. 11, 6793–6795.

[9]   Ya B Bazaliy and Andrzej Stankiewicz, *Ballistic (precessional) contribution to the conventional magnetic switching*, Appl. Phys. Lett. **98** (2011), no. 14, 142501–142501.

[10]   D. Bedau, H. Liu, J. J. Bouzaglou, A. D. Kent, J. Z. Sun, J. A. Katine, Eric E. Fullerton, and S. Mangin, *Ultrafast spin-transfer switching in spin valve*

nanopillars with perpendicular anisotropy, Appl. Phys. Lett. **96** (2010), no. 2, 022514.

[11] L. Berger, *Emission of spin waves by a magnetic multilayer traversed by a current*, Phys. Rev. B **54** (1996), 9353–9358.

[12] _____, *Effect of interfaces on gilbert damping and ferromagnetic resonance linewidth in magnetic multilayers*, J. Appl. Phys. **90** (2001), no. 9, 4632–4638.

[13] G. Bertotti, I. Mayergoyz, C. Serpico, and M. Dimian, *Comparison of analytical solutions of landau-lifshitz equation for "damping" and "precessional" switchings*, J. Appl. Phys. **93** (2003), no. 10, 6811–6813.

[14] G. Binasch, P. Grünberg, F. Saurenbach, and W. Zinn, *Enhanced magnetoresistance in layered magnetic structures with antiferromagnetic interlayer exchange*, Phys. Rev. B **39** (1989), 4828–4830.

[15] P. M. Braganca, I. N. Krivorotov, O. Ozatay, A. G. F. Garcia, N. C. Emley, J. C. Sankey, D. C. Ralph, and R. A. Buhrman, *Reducing the critical current for short-pulse spin-transfer switching of nanomagnets*, Appl. Phys. Lett. **87** (2005), no. 11, 112507.

[16] Yu A Bychkov and Emmanuel I Rashba, *Oscillatory effects and the magnetic susceptibility of carriers in inversion layers*, Journal of physics C: Solid state physics **17** (1984), no. 33, 6039.

[17] J. Cucchiara, Eric E. Fullerton, A. D. Kent, J. Z. Sun, Y. Henry, and S. Mangin, *Current-induced magnetization reversal in terms of power dissipation*, Phys. Rev. B **84** (2011), 100405.

[18] B. Dieny, V. S. Speriosu, S. S. P. Parkin, B. A. Gurney, D. R. Wilhoit, and D. Mauri, *Giant magnetoresistive in soft ferromagnetic multilayers*, Phys. Rev. B **43** (1991), 1297–1300.

[19] M. I. Dyakonov and V. I. Perel, *Current-induced spin orientation of electrons in semiconductors*, Phys. Lett. A **35** (1971), no. 6, 459–460.

[20] Xin Fan, Jun Wu, Yunpeng Chen, Matthew J Jerry, Huaiwu Zhang, and John Q Xiao, *Observation of the nonlocal spin-orbital effective field*, Nat. commun. **4** (2013), 1799.

70

[21] Albert Fert, Vincent Cros, J-M George, Julie Grollier, Henri Jaffres, A Hamzic, Annie Vaures, Giancarlo Faini, J Ben Youssef, and H Le Gall, *Magnetization reversal by injection and transfer of spin: experiments and theory*, J. Magn. Magn. Mater. **272** (2004), 1706–1711.

[22] G. D. Fuchs, N. C. Emley, I. N. Krivorotov, P. M. Braganca, E. M. Ryan, S. I. Kiselev, J. C. Sankey, D. C. Ralph, R. A. Buhrman, and J. A. Katine, *Spin-transfer effects in nanoscale magnetic tunnel junctions*, Appl. Phys. Lett. **85** (2004), no. 7, 1205–1207.

[23] Pietro Gambardella and Ioan Mihai Miron, *Current-induced spin–orbit torques*, Phil. Trans. R. Soc. A **369** (2011), no. 1948, 3175–3197.

[24] Thomas L Gilbert, *A phenomenological theory of damping in ferromagnetic materials*, Magnetics, IEEE Transactions on **40** (2004), no. 6, 3443–3449.

[25] Paul M. Haney, Hyun-Woo Lee, Kyung-Jin Lee, Aurélien Manchon, and M. D. Stiles, *Current induced torques and interfacial spin-orbit coupling: Semiclassical modeling*, Phys. Rev. B **87** (2013), 174411.

[26] Y. Henry, S. Mangin, J. Cucchiara, J. A. Katine, and Eric E. Fullerton, *Distortion of the stoner-wohlfarth astroid by a spin-polarized current*, Phys. Rev. B **79** (2009), 214422.

[27] J. E. Hirsch, *Spin hall effect*, Phys. Rev. Lett. **83** (1999), 1834–1837.

[28] Morris W Hirsch, Stephen Smale, and Robert L Devaney, *Differential equations, dynamical systems, and an introduction to chaos*, vol. 60, Academic press, 2004.

[29] Yiming Huai, Frank Albert, Paul Nguyen, Mahendra Pakala, and Thierry Valet, *Observation of spin-transfer switching in deep submicron-sized and low-resistance magnetic tunnel junctions*, Appl. Phys. Lett. **84** (2004), no. 16, 3118–3120.

[30] S. Ikeda, K. Miura, H. Yamamoto, K. Mizunuma, H. D. Gan, M. Endo, S. Kanai, J. Hayakawa, F. Matsukura, and H. Ohno, *A perpendicular-anisotropy cofeb–mgo magnetic tunnel junction*, Nature mater. **9** (2010), no. 9, 721–724.

[31] Y Jiang, T Nozaki, S Abe, T Ochiai, A Hirohata, N Tezuka, and K Inomata, *Substantial reduction of critical current for magnetization switching in an exchange-biased spin valve*, Nature Mater. **3** (2004), no. 6, 361–364.

[32] Mark Johnson and R. H. Silsbee, *Interfacial charge-spin coupling: Injection and detection of spin magnetization in metals*, Phys. Rev. Lett. **55** (1985), 1790–1793.

[33] Tomas Jungwirth, Jörg Wunderlich, and Kamil Olejník, *Spin hall effect devices*, Nature mater. **11** (2012), no. 5, 382–390.

[34] Alan Kalitsov, Mairbek Chshiev, Ioannis Theodonis, Nicholas Kioussis, and W. H. Butler, *Spin-transfer torque in magnetic tunnel junctions*, Phys. Rev. B **79** (2009), 174416.

[35] J. A. Katine, F. J. Albert, R. A. Buhrman, E. B. Myers, and D. C. Ralph, *Current-driven magnetization reversal and spin-wave excitations in co/cu/co pillars*, Phys. Rev. Lett. **84** (2000), 3149–3152.

[36] AD Kent, B Özyilmaz, and E Del Barco, *Spin-transfer-induced precessional magnetization reversal*, Appl. Phys. Lett. **84** (2004), no. 19, 3897–3899.

[37] Junyeon Kim, Jaivardhan Sinha, Masamitsu Hayashi, Michihiko Yamanouchi, Shunsuke Fukami, Tetsuhiro Suzuki, Seiji Mitani, and Hideo Ohno, *Layer thickness dependence of the current-induced effective field vector in ta/ cofeb/ mgo*, Nature mater. (2012).

[38] Kyoung-Whan Kim, Soo-Man Seo, Jisu Ryu, Kyung-Jin Lee, and Hyun-Woo Lee, *Magnetization dynamics induced by in-plane currents in ultrathin magnetic nanostructures with rashba spin-orbit coupling*, Phys. Rev. B **85** (2012), 180404.

[39] R. H. Koch, J. A. Katine, and J. Z. Sun, *Time-resolved reversal of spin-transfer switching in a nanomagnet*, Phys. Rev. Lett. **92** (2004), 088302.

[40] Alexey A. Kovalev, Arne Brataas, and Gerrit E. W. Bauer, *Spin transfer in diffusive ferromagnet-normal metal systems with spin-flip scattering*, Phys. Rev. B **66** (2002), 224424.

[41] D Lacour, JA Katine, N Smith, MJ Carey, and JR Childress, *Thermal effects on the magnetic-field dependence of spin-transfer-induced magnetization reversal*, Appl. Phys. Lett. **85** (2004), no. 20, 4681–4683.

[42] S. Le Gall, J. Cucchiara, M. Gottwald, C. Berthelot, C.-H. Lambert, Y. Henry, D. Bedau, D. B. Gopman, H. Liu, A. D. Kent, J. Z. Sun, W. Lin, D. Ravelosona, J. A. Katine, Eric E. Fullerton, and S. Mangin, *State diagram of nanopillar spin valves with perpendicular magnetic anisotropy*, Phys. Rev. B **86** (2012), 014419.

[43] Weiwei Lin, J. Cucchiara, C. Berthelot, T. Hauet, Y. Henry, J. A. Katine, Eric E. Fullerton, and S. Mangin, *Magnetic susceptibility measurements as a probe of spin transfer driven magnetization dynamics*, Appl. Phys. Lett. **96** (2010), no. 25, 252503.

[44] Huanlong Liu, Daniel Bedau, Dirk Backes, JA Katine, Jürgen Langer, and AD Kent, *Ultrafast switching in magnetic tunnel junction based orthogonal spin transfer devices*, Appl. Phys. Lett. **97** (2010), no. 24, 242510.

[45] Luqiao Liu, O. J. Lee, T. J. Gudmundsen, D. C. Ralph, and R. A. Buhrman, *Current-induced switching of perpendicularly magnetized magnetic layers using spin torque from the spin hall effect*, Phys. Rev. Lett. **109** (2012), 096602.

[46] Luqiao Liu, Takahiro Moriyama, D. C. Ralph, and R. A. Buhrman, *Spin-torque ferromagnetic resonance induced by the spin hall effect*, Phys. Rev. Lett. **106** (2011), 036601.

[47] Luqiao Liu, Chi-Feng Pai, Y Li, HW Tseng, DC Ralph, and RA Buhrman, *Spin-torque switching with the giant spin hall effect of tantalum*, Science **336** (2012), no. 6081, 555–558.

[48] A. Manchon and S. Zhang, *Theory of nonequilibrium intrinsic spin torque in a single nanomagnet*, Phys. Rev. B **78** (2008), 212405.

[49] _____, *Theory of spin torque due to spin-orbit coupling*, Phys. Rev. B **79** (2009), 094422.

[50] S Mangin, D Ravelosona, JA Katine, MJ Carey, BD Terris, and Eric E Fullerton, *Current-induced magnetization reversal in nanopillars with perpendicular anisotropy*, Nature Mater. **5** (2006), no. 3, 210–215.

[51] Stéphane Mangin, Y. Henry, D. Ravelosona, J. A. Katine, and Eric E. Fullerton, *Reducing the critical current for spin-transfer switching of perpendicularly magnetized nanomagnets*, Appl. Phys. Lett. **94** (2009), no. 1, 012502.

[52] Jan Manschot, Arne Brataas, and Gerrit E. W. Bauer, *Nonmonotonic angular magnetoresistance in asymmetric spin valves*, Phys. Rev. B **69** (2004), 092407.

[53] A. Matos-Abiague and R. L. Rodriguez-Suarez, *Spin-orbit coupling mediated spin torque in a single ferromagnetic layer*, Phys. Rev. B **80** (2009), 094424.

[54]   Ioan Mihai Miron, Kevin Garello, Gilles Gaudin, Pierre-Jean Zermatten, Marius V Costache, Stéphane Auffret, Sébastien Bandiera, Bernard Rodmacq, Alain Schuhl, and Pietro Gambardella, *Perpendicular switching of a single ferromagnetic layer induced by in-plane current injection*, Nature **476** (2011), no. 7359, 189–193.

[55]   Ioan Mihai Miron, Gilles Gaudin, Stéphane Auffret, Bernard Rodmacq, Alain Schuhl, Stefania Pizzini, Jan Vogel, and Pietro Gambardella, *Current-driven spin torque induced by the rashba effect in a ferromagnetic metal layer*, Nature materials **9** (2010), no. 3, 230–234.

[56]   Ioan Mihai Miron, Thomas Moore, Helga Szambolics, Liliana Daniela Buda-Prejbeanu, Stéphane Auffret, Bernard Rodmacq, Stefania Pizzini, Jan Vogel, Marlio Bonfim, Alain Schuhl, et al., *Fast current-induced domain-wall motion controlled by the rashba effect*, Nature Mater. **10** (2011), no. 6, 419–423.

[57]   Terunobu Miyazaki and N Tezuka, *Giant magnetic tunneling effect in fe/al2o3/fe junction*, Journal of Magnetism and Magnetic Materials **139** (1995), no. 3.

[58]   J. S. Moodera, Lisa R. Kinder, Terrilyn M. Wong, and R. Meservey, *Large magnetoresistance at room temperature in ferromagnetic thin film tunnel junctions*, Phys. Rev. Lett. **74** (1995), 3273–3276.

[59]   M. Morota, Y. Niimi, K. Ohnishi, D. H. Wei, T. Tanaka, H. Kontani, T. Kimura, and Y. Otani, *Indication of intrinsic spin hall effect in 4 d and 5 d transition metals*, Phys. Rev. B **83** (2011), 174405.

[60]   Shuichi Murakami, Naoto Nagaosa, and Shou-Cheng Zhang, *Dissipationless quantum spin current at room temperature*, Science **301** (2003), no. 5638, 1348–1351.

[61]   E. B. Myers, D. C. Ralph, J. A. Katine, R. N. Louie, and R. A. Buhrman, *Current-induced switching of domains in magnetic multilayer devices*, Science **285** (1999), no. 5429, 867–870.

[62]   Naoto Nagaosa, Jairo Sinova, Shigeki Onoda, AH MacDonald, and NP Ong, *Anomalous hall effect*, Rev. Mod. Phys. **82** (2010), no. 2, 1539.

[63]   Chi-Feng Pai, Luqiao Liu, Y Li, HW Tseng, DC Ralph, and RA Buhrman, *Spin transfer torque devices utilizing the giant spin hall effect of tungsten*, Applied Physics Letters **101** (2012), no. 12, 122404–122404.

[64] S. S. P. Parkin, C. Kaiser, A. Panchula, P. M. Rice, B. Hughes, M. Samant, and S. Yang, *Giant tunnelling magnetoresistance at room temperature with mgo (100) tunnel barriers*, Nat. Mater. **3** (2004), no. 12, 862–867.

[65] D. A. Pesin and A. H. MacDonald, *Quantum kinetic theory of current-induced torques in rashba ferromagnets*, Phys. Rev. B **86** (2012), 014416.

[66] S. Petit, C. Baraduc, C. Thirion, U. Ebels, Y. Liu, M. Li, P. Wang, and B. Dieny, *Spin-torque influence on the high-frequency magnetization fluctuations in magnetic tunnel junctions*, Phys. Rev. Lett. **98** (2007), 077203.

[67] Ung Hwan Pi, Kee Won Kim, Ji Young Bae, Sung Chul Lee, Young Jin Cho, Kwang Seok Kim, and Sunae Seo, *Tilting of the spin orientation induced by rashba effect in ferromagnetic metal layer*, Applied Physics Letters **97** (2010), no. 16, 162507–162507.

[68] D. C. Ralph and Mark D. Stiles, *Spin transfer torques*, J. Magn. Magn. Mater. **320** (2008), no. 7, 1190–1216.

[69] N. Reckers, J. Cucchiara, O. Posth, C. Hassel, F. M. Römer, R. Narkowicz, R. A. Gallardo, P. Landeros, H. Zähres, S. Mangin, J. A. Katine, E. E. Fullerton, G. Dumpich, R. Meckenstock, J. Lindner, and M. Farle, *Effect of microwave irradiation on spin-torque-driven magnetization precession in nanopillars with magnetic perpendicular anisotropy*, Phys. Rev. B **83** (2011), 184427.

[70] John Schliemann, *Spin hall effect*, Int. J. Mod. Phys. B **20** (2006), no. 09, 1015–1036.

[71] Takeshi Seki, Seiji Mitani, and Koki Takanashi, *Nucleation-type magnetization reversal by spin-polarized current in perpendicularly magnetized fept layers*, Phys. Rev. B **77** (2008), 214414.

[72] Jairo Sinova, Dimitrie Culcer, Q. Niu, N. A. Sinitsyn, T. Jungwirth, and A. H. MacDonald, *Universal intrinsic spin hall effect*, Phys. Rev. Lett. **92** (2004), 126603.

[73] J. C. Slonczewski, *Current-driven excitation of magnetic multilayers*, J. Magn. Magn. Mater. **159** (1996), no. 1, L1–L7.

[74] _____, *Excitation of spin waves by an electric current*, J. Magn. Magn. Mater. **195** (1999), no. 2, L261–L268.

[75] _____, *Currents, torques, and polarization factors in magnetic tunnel junctions*, Phys. Rev. B **71** (2005), 024411.

[76] JC Slonczewski, *Currents and torques in metallic magnetic multilayers*, J. Magn. Magn. Mater. **247** (2002), no. 3, 324–338.

[77] Inti Sodemann and Ya. B. Bazaliy, *Two scenarios of spin-transfer switching and criteria for the corresponding threshold currents*, Phys. Rev. B **84** (2011), 064422.

[78] M. D. Stiles, Jiang Xiao, and A. Zangwill, *Phenomenological theory of current-induced magnetization precession*, Phys. Rev. B **69** (2004), 054408.

[79] Edmund C. Stoner and E. P. Wohlfarth, *A mechanism of magnetic hysteresis in heterogeneous alloys*, Philosophical Transactions of the Royal Society of London. Series A. Mathematical and Physical Sciences (1948), 599–642.

[80] J. Z. Sun, *Current-driven magnetic switching in manganite trilayer junctions*, J. Magn. Magn. Mater. **202** (1999), no. 1, 157–162.

[81] J. Z. Sun and D. C. Ralph, *Magnetoresistance and spin-transfer torque in magnetic tunnel junctions*, J. Magn. Magn. Mater. **320** (2008), no. 7, 1227–1237.

[82] Gen Tatara and Hiroshi Kohno, *Theory of current-driven domain wall motion: Spin transfer versus momentum transfer*, Phys. Rev. Lett. **92** (2004), 086601.

[83] André Thiaville, *Coherent rotation of magnetization in three dimensions: A geometrical approach*, Phys. Rev. B **61** (2000), 12221–12232.

[84] M. Tsoi, A. G. M. Jansen, J. Bass, W.-C. Chiang, M. Seck, V. Tsoi, and P. Wyder, *Excitation of a magnetic multilayer by an electric current*, Phys. Rev. Lett. **80** (1998), 4281–4284.

[85] Ioan Tudosa, JA Katine, S Mangin, and Eric E Fullerton, *Perpendicular spin-torque switching with a synthetic antiferromagnetic reference layer*, Applied Physics Letters **96** (2010), no. 21, 212504.

[86] S. Urazhdin, Norman O. Birge, W. P. Pratt Jr, and J. Bass, *Switching current versus magnetoresistance in magnetic multilayer nanopillars*, Appl. Phys. Lett. **84** (2004), no. 9, 1516–1518.

[87] S. Urazhdin, H. Kurt, W. P. Pratt Jr, and J. Bass, *Effect of antiferromagnetic interlayer coupling on current-assisted magnetization switching*, Appl. Phys. Lett. **83** (2003), no. 1, 114–116.

[88] G. Vignale, *Ten years of spin hall effect*, J. Supercond. Nov. Magn. **23** (2010), no. 1, 3–10.

[89] Laurent Vila, Takashi Kimura, and YoshiChika Otani, *Evolution of the spin hall effect in pt nanowires: Size and temperature effects*, Phys. Rev. Lett. **99** (2007), 226604.

[90] Zihui Wang, Yiyan Sun, Mingzhong Wu, Vasil Tiberkevich, and Andrei Slavin, *Control of spin waves in a thin film ferromagnetic insulator through interfacial spin scattering*, Phys. Rev. Lett. **107** (2011), 146602.

[91] S. A. Wolf, D. D. Awschalom, R. A. Buhrman, J. M. Daughton, S. Von Molnar, M. L. Roukes, A. Y. Chtchelkanova, and D. M. Treger, *Spintronics: a spin-based electronics vision for the future*, Science **294** (2001), no. 5546, 1488–1495.

[92] Jiang Xiao, A. Zangwill, and M. D. Stiles, *Boltzmann test of slonczewskiâĂŹs theory of spin-transfer torque*, Phys. Rev. B **70** (2004), 172405.

[93] _____, *Macrospin models of spin transfer dynamics*, Phys. Rev. B **72** (2005), 014446.

[94] _____, *Spin-transfer torque for continuously variable magnetization*, Phys. Rev. B **73** (2006), 054428.

[95] Shu Yan and Ya. B. Bazaliy, *The switching phase diagrams and optimal switching of a perpendicular magnetic layer induced by spin hall effect*, in preparation.

[96] Shu Yan, Zhelin Sun, and Ya. B. Bazaliy, *Modification of the stoner-wohlfarth astroid by a spin-polarized current: An exact solution*, Phys. Rev. B **88** (2013), 054408.

[97] S. Yuasa, A. Fukushima, H. Kubota, Y. Suzuki, and K. Ando, *Giant tunneling magnetoresistance up to 410% at room temperature in fully epitaxial co/mgo/co magnetic tunnel junctions with bcc co(001) electrodes*, Appl. Phys. Lett. **89** (2006), no. 4, 042505–042505–3.

[98] S. Yuasa, T. Nagahama, A. Fukushima, Y. Suzuki, and K. Ando, *Giant room-temperature magnetoresistance in single-crystal fe/mgo/fe magnetic tunnel junctions*, Nat. Mater. **3** (2004), no. 12, 868–871.

[99] S. Zhang, P. M. Levy, and A. Fert, *Mechanisms of spin-polarized current-driven magnetization switching*, Phys. Rev. Lett. **88** (2002), 236601.

[100] Shufeng Zhang, *Spin hall effect in the presence of spin diffusion*, Phys. Rev. Lett. **85** (2000), 393–396.

[101] Ru Zhu and Pieter B Visscher, *Spin torque switching in perpendicular films at finite temperature*, J. Appl. Phys. **103** (2008), no. 7, 07A722–07A722.

APPENDIX A

CLASSIFICATION OF EQUILIBIRUM TYPES

Table A.1: Classification of stabilities

Stability Type	Equilibrium Type	Eigenvalue Equivalent	tr$A$-det$A$ Equivalent	λ Equivalent
Sink	Stable focus Stable node	Complex Re$[\mu_\pm] < 0$ Real $\mu_- < \mu_+ < 0$	tr$A < 0$, det$A > 0$	$\begin{cases} \lambda > \mathrm{Max}(\lambda_{\mathrm{T}}, \lambda_+) & \text{if } \lambda_{\mathrm{T}} \geqslant \lambda_- \\ \lambda_{\mathrm{T}} < \lambda < \lambda_- & \text{if } \lambda_{\mathrm{T}} < \lambda_- \end{cases}$
Source	Unstable focus Unstable node	Complex Re$[\mu_\pm] > 0$ Real $0 < \mu_- < \mu_+$	tr$A > 0$, det$A > 0$	$\begin{cases} \lambda < \mathrm{Min}(\lambda_{\mathrm{T}}, \lambda_-) & \text{if } \lambda_{\mathrm{T}} \leqslant \lambda_+ \\ \lambda_+ < \lambda < \lambda_T & \text{if } \lambda_{\mathrm{T}} > \lambda_+ \end{cases}$
Saddle	Saddle point	Real $\mu_- < 0 < \mu_+$	det$A < 0$	$\lambda_- < \lambda < \lambda_+$
Center	Center	Imaginary	tr$A = 0$	$\lambda = \lambda_{\mathrm{T}}$

Table A.2: Classification of focus and node

Equilibrium Type	Eigenvalues	tr$A$-det$A$ Equivalent	λ Equivalent
Node	Real eigenvalues	$(\mathrm{tr}A)^2 - 4\mathrm{det}A > 0$, det$A > 0$	$\lambda_{c-} < \lambda < \lambda_-$ or $\lambda_+ < \lambda < \lambda_{c+}$
Focus	Complex eigenvalues	$(\mathrm{tr}A)^2 - 4\mathrm{det}A < 0$ (det$A > 0$ satisfied)	$\lambda < \lambda_{c-}$ or $\lambda > \lambda_{c+}$

Appendix B

Graphic method for equilibrium finding

In order to find the equilibria, we need to solve (4.7) for an arbitrary external field. The field is confined in xz plane without loss of generality, $\mathbf{h} = (h_x, 0, h_z)$. Express both sides in Cartesian coordinates and after some arrangement, we get

$$
\begin{aligned}
h_x \sin\phi &= h_{\text{st}} - \frac{1}{\sin\theta}\frac{\partial\varepsilon}{\partial\phi} \;, \\
h_x \cos\phi &= \lambda \sin\theta + \cos\theta\frac{\partial\varepsilon}{\partial\phi} \;, \\
h_z &= \lambda \cos\theta - \sin\theta\frac{\partial\varepsilon}{\partial\phi} \;.
\end{aligned}
\tag{B.1}
$$

In Stoner-Wohlfarth model with the anisotropy energy given by (4.2), Eqs. (B.1) can be calculated as

$$
\begin{aligned}
h_x \sin\phi &= h_{\text{st}} \;, \\
h_x \cos\phi &= (\lambda + \cos^2\theta)\sin\theta \;, \\
h_z &= (\lambda - \sin^2\theta)\cos\theta \;.
\end{aligned}
\tag{B.2}
$$

The angle ϕ is also a function of θ and can be eliminated by combining the first two equations in (B.2). If we further require $h_x \geqslant 0$, then we can get

$$
\begin{aligned}
h_x &= \sqrt{(\lambda + \cos^2\theta)^2 \sin^2\theta + h_{\text{st}}^2} \;, \\
h_z &= (\lambda - \sin^2\theta)\cos\theta \;.
\end{aligned}
\tag{B.3}
$$

The two equations in (B.3) express h_x and h_z as functions of λ. In turn, we can also write λ as functions of h_x and h_z, respectively. We name the two functions $\Lambda_\pm$ and Λ_z

$$\Lambda_\pm(\theta) \;=\; \pm\frac{1}{\sin\theta}\sqrt{h_x^2 - h_{\mathrm{st}}^2(\cos\theta)} - \cos^2\theta, \tag{B.4a}$$

$$\Lambda_z(\theta) \;=\; \frac{1}{\cos\theta}h_z + \sin^2\theta. \tag{B.4b}$$

The $\pm$ sign in (B.4a) indicates the corresponding equilibria are on the $+x$ and $-x$ hemispheres, respectively. The equilibria can be obtained numerically by equating the two equations above

$$\Lambda_\pm = \Lambda_z. \tag{B.5}$$

A straightforward way to understand the method is to plot them on the critical λ graph. On the λ graph, the equilibria are presented by the intersection points of $\Lambda_\pm$ and Λ_z, which means that their stabilities as well as the angles can be read directly from the graph (see Fig. B.1). The different destabilization scenrios can be seen easily by tracking all the equilibria when $\mathbf{h}$ is moving along a path that crosses different parts of the critical curve.
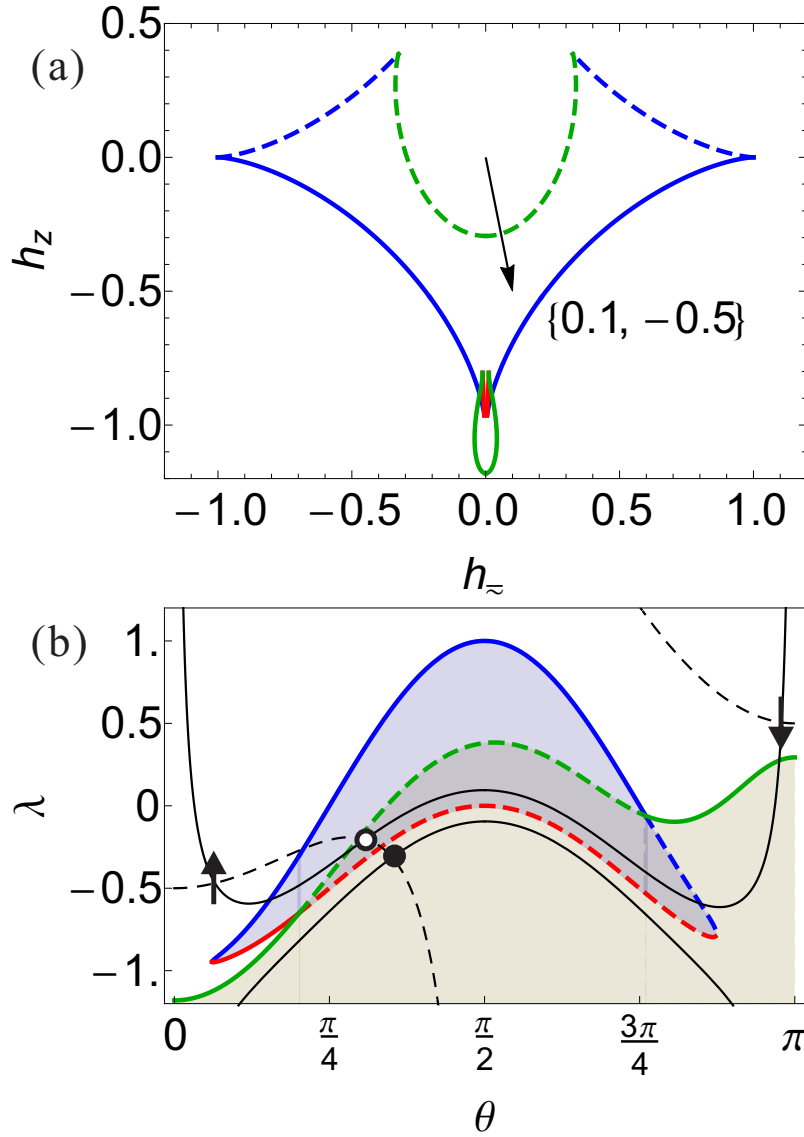
Figure B.1: Graphic method for determine equilibria in the λ-θ plane. (a) the applied field is inside the modified astroid with $j/j_0 = 0.1$, (b)the intersections of $\Lambda_\pm$ (solid black curves) and Λ_z (dashed black curves) correspond to the equilibria. The four equilibria are two stable equilibria (parallel and antiparallel labeled by the arrows), one unstable equilibria (dot) and one saddle point (circle).